UNIVERSITY OF PAVIA
FACULTY OF ENGINEERING

UNIVERSITY SCHOOL OF ADVANCED STUDIES - IUSS PAVIA

Modelling Rock-Ice Avalanches: Application of the Physically Based Model RAMMS to the Solatset Glacier, Valpelline, Italy

A Thesis Submitted in Partial Fulfilment of the Requirements

for the Degree of Master of Science (Laurea Magistrale) in

Civil Engineering for the Mitigation of Risk from Natural Hazards

by

Anne-Kathrin Kappler

Supervisors: Prof. Dr. Massimiliano Barbolini, Prof. Dr. Marco Pasian

Assistant Supervisor: Dr. Perry Bartelt

April, 2026

ABSTRACT

This research investigates whether, and to what extent, inherent uncertainties in the simulation of complex natural processes influence the behaviour of rock–ice avalanches, with a particular focus on runout distances and potentially affected areas. For summer scenario variations in initial water content in the unstable glacier mass are analysed using physically based simulations generated with the RAMMS modelling framework, followed by a statistical sensitivity analysis of model outcomes. For winter scenario the same modelling framework is used to evaluate the effects of different snow cover depths over the glacier and along the flow path.
A review of the literature shows that, while statistical approaches have been applied to other mass-movement processes, a dedicated statistical evaluation of rock–ice avalanche dynamics is still lacking. Simulating such hazardous events is increasingly important due to accelerated glacier retreat, which alters thermal and hydrological conditions. In the European Alps, where these events occur in densely populated regions, understanding rock–ice avalanche dynamics is essential for hazard assessment. Compared to seasonal snow avalanches, rock–ice avalanches are characterized by greater volume, density, and harmful consequences.
The study focuses on the Solatset Glacier in the Aosta Valley, Italy whereas the Marmolada glacier collapse from 2022 was used as a reference event to calibrate friction parameters and relevant physical properties. Based on this, four release scenarios for the Solatset Glacier were simulated, representing different seasonal conditions and release volumes.

Keywords: alpine mass movement, glacier hazards, climate change, rock-ice avalanche, numerical simulations, statistical analysis

ACKNOWLEDGEMENTS

I would like to express my sincere gratitude to Fondazione Montagna Sicura (FMS) for providing the initial material necessary for this research. In particular, I acknowledge the provision of the glacier outlines from 2000 and 2008, as well as the glacier thickness data and the digital elevation model (DEM), which formed the essential basis for the analyses carried out in this thesis.

I am also deeply grateful to the team of RAMMS, especially Marc Christen and Dr. Perry Bartelt, for providing access to the RAMMS software and for their valuable supervision and support throughout the working phase of this project. Their expertise, guidance, and constructive feedback were fundamental to the successful development of this research. I would like to thank my professors, in particular Prof. Dr. Massimiliano Barbolini, Prof. Dr. Marco Pasian, and Dr. Francesco Stefanini, for their guidance, availability, and support throughout my academic journey and during the development of this thesis. Their teaching and scientific insight have greatly contributed to my growth as a student and researcher.

Finally, I would like to thank my family, my boyfriend and my friends (Kimiya and Ali) for their constant encouragement, patience, and support throughout my studies. Their belief in me and their unwavering support made this achievement possible.

TABLE OF CONTENTS

LIST OF FIGURES

LIST OF TABLES

LIST OF SYMBOLS

Φ	= avalanche core
Π	=suspension cloud
$\hat{h}_{\phi}$	= total-depth average height
$\hat{\rho}_{\phi}$	= co-volume density of core
$\hat{h}_{\alpha}$	= depth-averaged component height
h_{ϕ}	= flowing height of core
ρ_{α}	= constant component bulk density
m_{α}	= component mass
h_{α}	= flowing height of each component
$\vec{u}_{\phi}$	= mean slope-parallel velocity of core
ρ_{Σ}	= density entrained material
$\hat{\rho}_{\Pi}$	= co-volume density of cloud
$\dot{M}_{\Sigma\to\phi}$	= entrainment of path materials into the avalanche core
$\dot{M}_{\phi\to\Pi}$	= core mass injected into the dust cloud
$\dot{M}_{\phi\to\Pi_r}$	= rock mass injected into the dust cloud
$\dot{M}_{\phi\to\Pi_i}$	= ice mass injected into the dust cloud
$\hat{h}_r, \hat{h}_i, \hat{h}_s, \hat{h}_w$	= co-volume height of rock, ice, snow, and water in the core
ρ_r, ρ_s, ρ_w	= density of rock, snow, and water
$\eta_r, \eta_i, \eta_s, \eta_w$	= mass fraction of rock, ice, snow, and water in the entrained material
υ_r, υ_i	= volumetric fraction of rock-dust, and ice-dust
$\dot{Q}_{m_i}, \dot{Q}_{m_s}, \dot{Q}_{m_w}$	= energy required to melt the ice, the snow or the water

L = latent heat of fusion of the ice

θ_i, θ_s = volumetric fraction of ice, and snow in the core

p_ϕ = basal pressure

I = two-dimensional unity matrix

$\vec{G}$ = driving force of gravity

S_ϕ = shearing resistance of the avalanche core

R_ϕ = granular temperature

$\vec{u}_\phi{}'$ = mean slope-parallel velocity of the core

a_ϕ = splitting factor to separate the shearing work within the core

$\dot{W}_\phi$ = shear work

β_ϕ = decay parameter for the fluctuation energy of the core

μ_D = lubricated friction coefficient of the core

N_ϕ = basal normal stress

N_0 = normal stress

$\xi_\phi, \xi_r, \xi_{is}, \xi_w$ = lubricated, rock, ice, and water turbulent coefficient of the core

A_ϕ, A_r, A_i, A_s = activation energy of core, rock, ice and snow

ϕ_r, ϕ_i, ϕ_s = mass fraction of rock, ice, and snow in the core

e_r, e_w, e_i = internal heat energy and temperature of the rock, water, and ice

$\dot{E}_\phi$ = total heat energy produced in the core

$\dot{E}_{\Sigma\to\phi}$ = internal energy produced during the entrainment process

$\dot{q}_{ri}, \dot{q}_{rw}, \dot{q}_{iw}$ = sensible heat exchanges between the rock/ice/water mixture

P = impact probability

Cw = volumetric water content

Sc = critical saturation

Θ = difference between ice temperature and melting temperature of ice

ρb = snow density

1. INTRODUCTION

Ongoing global climate change poses increasing challenges for mountainous regions worldwide. The retreat of glaciers and the degradation of permafrost significantly alter slope stability, hydrological regimes, and geomorphological processes. These changes give rise to new dynamics and emerging natural hazards that require systematic investigation and monitoring.

At present, approximately 10% of the Earth's land surface is covered by one of the most sensitive indicators of global warming, the glacier. While the majority of glaciers are located within the arctic circle in the form of ice sheets, a substantial number of glaciers are distributed across high mountain regions worldwide (Cuffey and Paterson, 2010).

Since the end of the last Ice Age, and particularly since the beginning of the 21st century, global glacier retreat has accelerated markedly. Between 2000 and 2019, glaciers worldwide lost on average approximately 267 billion tonnes of ice per year (ETH Zurich, 2021).

These rapid changes in the cryosphere affect not only the glaciers themselves but also the broader Earth system, influencing interactions between the hydrosphere, atmosphere, biosphere, and lithosphere (Benn and Evans, 2010).

The consequences are particularly visible looking at the example of the European alps in which glaciers have a central impact on the landscape. They release water, scout the bedrock, cooling water during the summer or providing habitat for many species (Cuffey and Paterson, 2010).

In addition to glacier retreat, atmospheric warming leads to permafrost degradation. Rising ground temperatures reduce the mechanical stability of ice-bonded rock masses, thereby increasing the frequency of slope instabilities such as rockfalls and debris flows in high-mountain environments. Furthermore, these processes enhance the likelihood of ice avalanches and, in particular, rock–-ice avalanches (Jacquemart et al., 2024).

Research has shown that between 2007 and 2017 the temperature of permafrost layers has increased by 0.3°C , globally (Noetzli et al., 2006).

Considering these changing surroundings the introductory chapters will outline the topic of ice & rock avalanches and will provide evidence for the existence of hazardous and devastating effects of these occurrences.

2. AIM OF THE THESIS

The aim of the thesis is to investigate whether, and to what extent inherent uncertainties in the simulation of complex natural processes influence the behaviour of rock-ice avalanches, especially the run-out distance. Variations in initial water and ice fractions as well as snow depth have been investigated. The study is based on physically derived simulation results obtained using the RAMMS (Rapid Mass Movement Simulation) modelling framework, followed by a statistical analysis of parameter sensitivities.

A comprehensive review of the literature revealed that, while statistical approaches have been applied to other mass–movement processes, no studies to date have focused on a statistical evaluation of rock–ice avalanche dynamics.

The numerical simulations in this study were carried out using the RAMMS software with the extension for rock–ice avalanches. RAMMS is a well-established, physically based modelling framework that has been widely applied to simulate gravitational mass movements in complex alpine terrain. The rock–ice avalanche module builds upon recent developments in dynamic thermo-mechanical modelling and is described in detail by Munch et al. (2024) (chapter five).

By addressing the lack of statistical evaluation within rock–ice avalanche modelling, this study contributes a quantitative framework for assessing the influence of initial material composition on avalanche dynamics. The area of interest is located at the Solatset Glacier in the Aosta Valley, Italy.

The need to simulate potentially dangerous events such as ice-rock avalanches arise from the fact that glacier retreat has accelerated dramatically, modifying thermal conditions and hydrological dynamics (UZH, 2007). It is increasingly important to find a way to manage and predict possible situations dangerous for humans frequenting high mountain environments.

The spatial distribution of documented rock–ice avalanches suggests a concentration in northwestern North America and the European Alps, although this pattern may partly reflect regional differences in documentation and data availability (Schneider et al., 2011). A

closer examination of the map (Figure 2.1) supports these findings. Additionally, it reveals that High Mountain Asia, which contains approximately 95 500 glaciers over an area of about 100 000 km^2, has also experienced numerous large-scale events (Zhong et al., 2024).

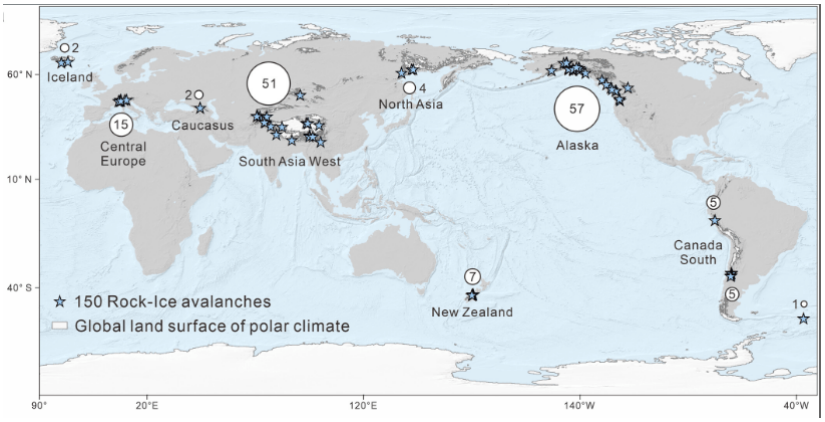

Figure 2.1: Spatial distribution of rock-ice avalanches (Fan et al., 2025)

Several recent events illustrate the destructive potential of large rock–ice avalanches. In May 2025, the collapse of the Birch Glacier mobilized approximately 10 million m^3 of material, destroying parts of the village of Blatten and temporarily damming the local river (Farinotti et al., 2025). A particularly large and complex event occurred in 2002 at the Kolka Glacier in the Caucasus Mountains, where approximately 130 million m^3 of rock and ice were mobilized and travelled nearly 20 km (Evans et al., 2009). In central Himalaya, three major events between 2012 and 2021 resulted in 622 fatalities, underscoring the substantial human impact associated with such processes (Zhong et al., 2024).

Since rock-ice avalanches in the European alps happen in a region which is densely populated and highly developed, compared to other high mountain areas in the world, we must understand the principles and hazards coming from these types of avalanches to improve the protection.

The rock–ice avalanche is a particular type of the ice avalanche, which is marked by an increased volume, density and flow speed (UZH, 2007). Although rock-ice avalanches continue to rise as a threat for high mountainous regions our understanding of their initiation and internal processes remains limited, mainly due to their complexity. Starting zones of rock-ice avalanches can be categorized as cliff-type or ramp-type failures (Huggel, Kääb, and Haeberli, 2004), which can happen due to the fact of missing adhesion at the glacier

bed, low lateral support on channel-shaped beds, or missing support by parts which are frozen to the glacier bed. Researchers such as Röthlisberger (1987) point out the difficulty of predicting the stability of mountain slopes (Alean, 1985). Detachment of the mass within Cliff-type glaciers can be linked to extending flow as well as crevasse formation, primarily due to significant tensile stresses. Whereas ramp-type glaciers involving instability at the depth where the ice-rock interface could be found as well as a critical value for the slope angle of the glacier bed (Noetzli et al., 2006).
The distinct characteristic of rock-ice avalanches is the shattering and friction in the transition and deposition area (Alean, 1985).

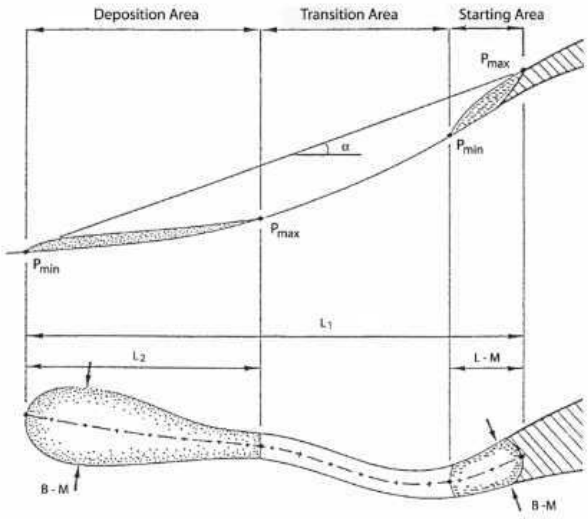

Figure 2.2: Starting, transition and deposition area of ice avalanches (Alean, 1985)

Throughout an avalanche event, ice continually shatters, generating a considerable amount of ice powder as well as smaller particles (UZH, 2007). Laboratory experiments show that the friction coefficient decreases linearly with increasing ice content, resulting in approximately a 20% reduction in friction for dry granular pure ice compared to gravel alone. This is attributed to the potential interaction and transformation of ice, snow and water and increases the potential for damage and casualties for such avalanches.
Temperature plays an important role in influencing the stability condition and the critical slope. Research indicates that an increase in ground temperature could lead to a decrease in shear strength of ice-bounded discontinuities, thus lowering the slope safety factor (Noetzli et al., 2006). Since the temperature of ice and snow are very close to their melting tem-

perature, even small changes are likely to generate a large impact on the amount of water produced during the avalanche, but also within and at the glacier's foundation (Fan et al., 2025).

Combined rock-ice avalanches can get triggered by major rock falls onto the glacier that keep and release large volumes of rock and ice. These rockfalls but also rock-ice avalanches can be triggered from the melting of ice-filled rock joints, leading to an increase of water pressure. All of these triggers are directly connected to the presented factors of global warming and represent a newly rising danger for alpine regions. Catastrophic chain reactions can happen if the deposit area is snow covered or consists of a lake. It can trigger a snow avalanche or lake burst, posing serious danger to nearby populations (UZH, 2007).

3. STATE OF THE ART

Rock–-ice avalanches have been recognized as a significant natural hazard for several decades. Their potential impacts, not only in the European Alps but also in high-mountain regions worldwide, have been extensively discussed in the scientific literature.

Since the early 2000s, numerous studies have addressed the driving mechanisms, hazard potential, and mobility of such events. Notable examples include *"Unravelling driving factors for large rock–ice avalanche mobility"* by Schneider et al. (2011), *"An assessment procedure for glacial hazards in the Swiss Alps"* by Huggel, Kääb, and Haeberli (2004), *"Imminent threat of rock–ice avalanches in High Mountain Asia"* by Fan et al. (2022), and *Large rock and ice avalanches frequently produce cascading processes in High Mountain Asia"* by Zhong et al. (2024).

In addition to observational and hazard-focused studies, numerical modelling of rock–-ice avalanches using modern simulation tools has also received considerable attention. Early work by Noetzli et al. (2006), published in Computers & Geosciences, introduced *"GIS-based modelling approaches for rock–ice avalanches originating from alpine permafrost areas"*. More recently, Munch et al. presented a dynamic thermo-mechanical modelling framework for rock–ice avalanches in *JGR Earth Surface*, employing a newly developed extension of the RAMMS software specifically designed to capture flow transitions, water dynamics, and associated uncertainties.

The aim of this thesis is to apply a statistical analysis to investigate whether, and to what extent, variations in initial water and ice fractions influence run-out distance, velocity, and powder pressure. A comprehensive review of the literature revealed that, while statistical approaches have been applied to other mass-movement processes, no studies to date have focused on a statistical evaluation of rock–ice avalanche dynamics. For example,Barbolini and Savi (2001) applied statistical methods to snow avalanche hazard assessment, but their analysis did not address rock–ice avalanches. By addressing this gap, the present study contributes a novel perspective to rock–ice avalanche research and provides a quantitative framework for assessing the influence of initial material composition on avalanche behaviour.

4. DESCRIPTION OF THE STUDY AREA

This study examines the Solatset Glacier, situated in the Aosta Valley near Valpelline, Italy. Recent Google Earth imagery from summer 2025 provides a clear view of the glacier.

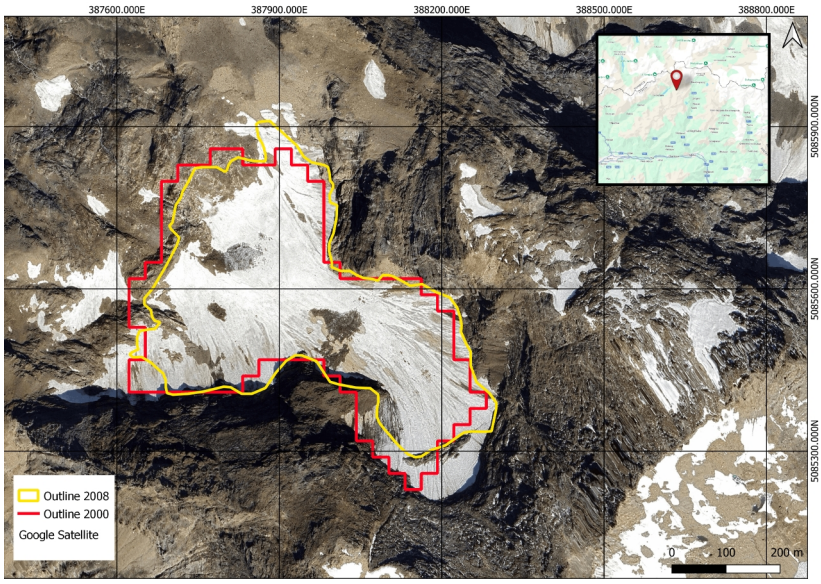

Figure 4.1: Solatset glacier outline 2000 (red) and 2008 (yellow)

Located within the Pennine Alps, it is framed by Monte Dragone (3,354 m) and Punta di Fontanella (3,384 m). The glacier extends from approximately 3,110 m at its highest point to about 2,760 m at its lowest, with an average slope close to 30°. Its orientation is toward the northeast. As of summer 2025, the Solatset Glacier reaches a maximum length of around 700 m and a width of up to 550 m. The retreat of the glacier becomes visible looking at the outlines from 2000 and 2008 in Fig. 4.1. Furthermore, historical satellite images (Google, 2026) show a progressive loss of ice mass. Compared to 2009 the satellite images show a decrease in length by about 50m and width by around 100m.

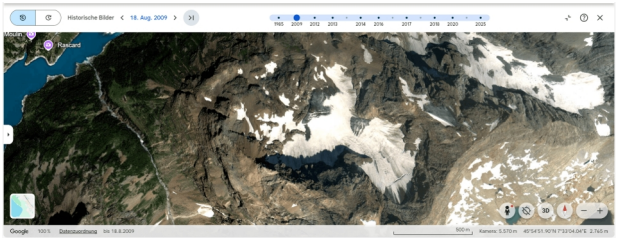

Figure 4.2: Historical satellite image of the Solatset glacier from 18.08.2009

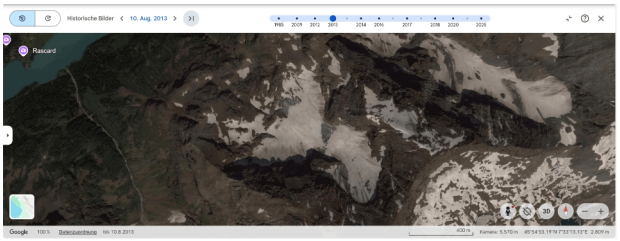

Figure 4.3: Historical satellite image of the Solatset glacier from 10.08.2013

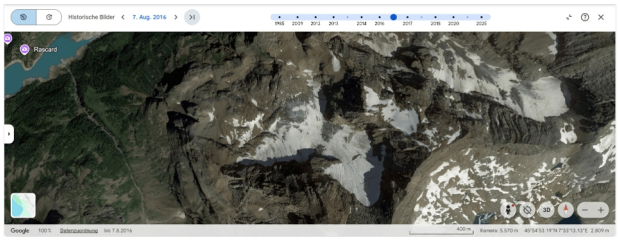

Figure 4.4: Historical satellite image of the Solatset glacier from 07.08.2016

These results are consistent with regional observations and broader research on climate change impacts. North-West Italy, the Aosta valley experienced an active layer thickening and warming of around 0.2°C/yr. Observed at a depth of 15m at an elevation of 3500m (Jacquemart et al., 2024). The Solatset Glacier is classified as a cirque glacier, having developed within a bowl-shaped mountain hollow. Seracs are visible (Giani, 2026).

4.1 OBJECTS OF IMAPCT

If an avalanche were to occur due to a collapse of the Solatset Glacier, the resulting cascade of impacts could be severe. The glacier lies directly above Place Moulin Lake, an artificial reservoir created by the construction of a dam between 1955 and 1965. The reservoir holds approximately 105 million m^3 of water and is supplied by a 137 km^2 catchment area, nearly 20% of which is glacierized. The dam impounds the Buthier River, a tributary of the Dora Baltea (Bionaz, 2025). A large avalanche entering the lake could trigger a displacement wave,

potentially causing overtopping or structural stress on the dam, which in turn may lead to a lake outburst and downstream flooding.

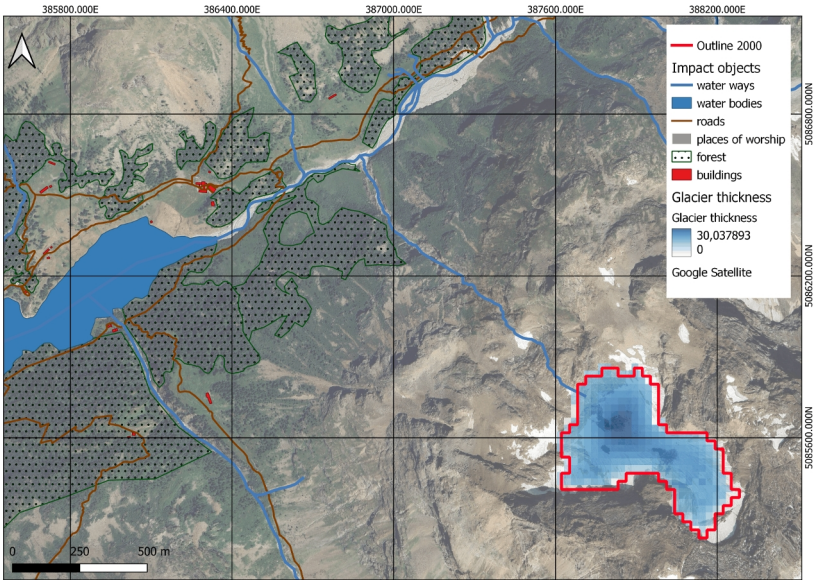

Figure 4.5: Objects of impact

The Solatset Glacier is additionally surrounded by elements that could be affected in the event of an avalanche, potentially contributing to significant damage. The identified objects at risk include,

- Hiking trails
- Rifugio Prarayer
- Forest around the lake
- Several buildings around the lake

and are visible in Figure 4.5.

5. METHODOLOGY & MATERIALS

The analysis is based on the glacier outline from the year 2000, as well as glacier thickness data and a DEM provided by FMS.

5.1 RAMMS MODEL DESCRIPTION

In this study, rock-ice avalanches are simulated using the RAMMS software, which implements a depth-averaged, two-phase modelling approach to capture the dynamics of both the dense avalanche core (ϕ) and the overlying suspension cloud (Π). The avalanche core is treated as a multi-component mixture of rock (r), ice (i), water (w) and snow (s), where each component contributes to the total-depth-averaged height ($\hat{h}_\phi$) and the co-volume density ($\hat{\rho}_\phi$). The temporal evolution of the core is described using coupled mass and momentum conservation equations. Flow heights of both the core and the cloud are measured normal to the basal surface, while velocity vectors are defined parallel to the slope as shown in Fig.5.1.

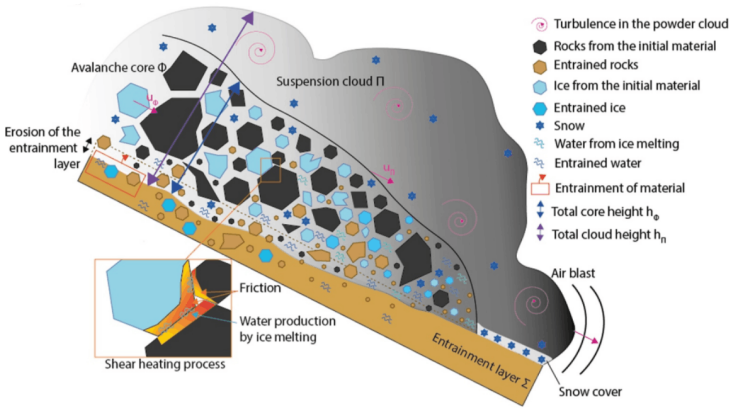

Figure 5.1: Components of the core and stresses applied to it (Munch et al., 2024)

The mass of each component (α) is defined as the product of a depth-averaged component height ($\hat{h}_\alpha$) and a constant bulk density (ρ_α).

$$m_\alpha = h_\alpha \, \hat{\rho}_\alpha \tag{5.1}$$

The total core height is then given by,

$$\hat{h}_\phi = \sum_\alpha \frac{\rho_\alpha}{\hat{\rho}_\phi} \, \hat{h}_\alpha \tag{5.2}$$

reflecting the combined contribution of all components.
Entrainment and mass exchange processes are included through source terms with the dimension of velocity within the mass balance equations:

$$\frac{\partial \hat{h}_\phi}{\partial t} + \nabla \cdot \left(\hat{h}_\phi \, \vec{u}_\phi \right) = \frac{\rho_\Sigma}{\hat{\rho}_\phi} \, \dot{M}_{\Sigma \to \phi} - \frac{\rho_\Pi}{\hat{\rho}_\phi} \, \dot{M}_{\phi \to \Pi} \tag{5.3}$$

$$\frac{\partial \hat{h}_\phi}{\partial t} + \nabla \cdot \left(h_\phi \, \vec{u}_\phi \right) = D(x,t) \tag{5.4}$$

These terms represent both the entrainment of basal material into the core $\dot{M}_{\Sigma \to \phi}$ and the transfer of fine particles from the core to the dust cloud $\dot{M}_{\phi \to \Pi}$. The function $D(x,t)$ describes the change of the avalanche core height due to dispersive pressure.
Four additional component-specific mass balance equations are solved since the volumetric contents of rock, ice, snow and water are tracked separately.

$$\partial_t \hat{h}_r + \nabla \cdot \left(\hat{h}_r \, \vec{u}_\phi \right) = \frac{\rho_\Sigma}{\rho_r} \, \eta_r \, \dot{M}_{\Sigma \to \phi} - \upsilon_r \, \dot{M}_{\phi \to \Pi_r} \tag{5.5}$$

$$\partial_t \hat{h}_i + \nabla \cdot \left(\hat{h}_i \, \vec{u}_\phi \right) = \frac{\rho_\Sigma}{\rho_r} \, \eta_i \, \dot{M}_{\Sigma \to \phi} - \frac{\dot{Q}_{m_i}}{\rho_i \, L} - \frac{\theta_i}{\theta_i + \theta_s} \, \upsilon_i \, \dot{M}_{\phi \to \Pi_i} \tag{5.6}$$

$$\partial_t \hat{h}_s + \nabla \cdot \left(\hat{h}_s \, \vec{u}_\phi \right) = \frac{\rho_\Sigma}{\rho_s} \, \eta_s \, \dot{M}_{\Sigma \to \phi} - \frac{\dot{Q}_{m_s}}{\rho_s \, L} - \frac{\theta_s}{\theta_i + \theta_s} \, \frac{\rho_i}{\rho_s} \, \upsilon_i \, \dot{M}_{\phi \to \Pi_i} \tag{5.7}$$

$$\partial_t \hat{h}_w + \nabla \cdot \left(\hat{h}_w \, \vec{u}_\phi \right) = \frac{\rho_\Sigma}{\rho_w} \, \eta_w \, \dot{M}_{\Sigma \to \phi} - \frac{\dot{Q}_{m_w}}{\rho_w \, L} \tag{5.8}$$

The momentum conservation accounts for gravitational acceleration, pressure gradients, and basal friction.

$$\partial_\phi\Big(\hat{h}_\phi\,\vec{u}_\phi\Big) + \nabla\cdot\Big(\hat{h}_\phi\,\vec{u}_\phi\otimes\vec{u}_\phi + p_\phi\,I\Big) = \vec{G}\,\hat{h}_\phi - \frac{\vec{u}_\phi}{\|\vec{u}_\phi\|}\,S_\phi - \frac{\hat{\rho}_\Pi}{\hat{\rho}_\phi}\,\dot{M}_{\phi\to\Pi}\,\vec{u}_\phi \tag{5.9}$$

The basal pressure is assumed to be hydrostatic with respect to the flowing density of the core. To capture the fluidization of the avalanche core, the model introduces, among others, the concept of granular temperature (R_ϕ), which quantifies the kinetic energy associated with particle fluctuations.

$$R_\phi = \frac{\hat{\rho}_\phi}{2}\,\left\|\vec{u}'_\phi\right\|^2 \tag{5.10}$$

The evolution of granular temperature is governed by:

$$\partial_t\Big(\hat{h}_\phi\,R_\phi\Big) + \nabla\cdot\Big(\hat{h}_\phi\,R_\phi\,\vec{u}_\phi\Big) = \dot{P}_\phi = a_\phi\,\dot{W}_\phi - M_{\phi\to\Pi}\,R_\phi - \hat{h}_\phi\,R_\phi\,\beta_\phi \tag{5.11}$$

where the primary source of velocity fluctuations and enhanced flow mobility is shear work ($\dot{W}_\phi$) of which only a fraction, $a_\phi < 1$, is converted into fluctuation energy, while the remainder is dissipated directly as heat.

Furthermore, the basal shear stress (S_ϕ) is parameterized using the Voellmy friction law, with μ_ϕ as the Coulomb friction coefficient and ξ_ϕ as the velocity-squared turbulent parameter. Both terms depend on the evolving state of the mixture, including water content and degree of fluidization. Therefore, the Coulomb friction coefficient is adjusted as a function of water content following an exponential law. Additionally, a non-linear relationship between shear stress and normal stress is introduced to account for experimental observations in granular and snow flows. This adjustment yields the final expression for basal shear resistance.

$$S_\phi = \mu_D\,N_\phi + (1-\mu_D)\,N_0\left[1-\exp\!\left(-\frac{N_\phi}{N_0}\right)\right] + \rho_\phi\,g\,\frac{\|\vec{u}_\phi\|^2}{\xi_\phi} \tag{5.12}$$

Granular fluidization is parameterized using activation energies (A_ϕ) that quantify the shear work required to fluidize rock, ice, and snow.

$$A_\phi = \Phi_r A_r + \Phi_i A_i + \Phi_s A_s \tag{5.13}$$

Empirical studies suggest that activation energy increases from snow to ice and from ice to

rock.

In general, it can be said that fluidization leads to an increase in the effective flow height $\hat{h}_\phi$. The true flow height (h_ϕ) is therefore defined as a dilated height that includes additional pore space filled with entrained air.

Properties for the height and density of the flow at rest are implemented as follows:

$$h_\phi \geq \hat{h}_\phi \qquad \text{and} \qquad \rho_\phi \leq \hat{\rho}_\phi \tag{5.14}$$

The avalanche cloud is described using analogous height and density variables. In this case, the true height additionally accounts for air entrainment driven by turbulent motions at the cloud boundaries.

The production of meltwater is a key thermodynamic process in rock-ice avalanches. The rate of meltwater generation is given by a source term in the water mass balance equation:

$$\frac{\dot{Q}_m}{\rho_w L} \tag{5.15}$$

The required latent heat is computed based on the densities and latent heat capacities of snow and ice, defining melting by these terms:

$$\frac{\dot{Q}_{m_s}}{\rho_s L} \qquad \text{and} \qquad \frac{\dot{Q}_{m_i}}{\rho_i L} \tag{5.16}$$

It is assumed that snow melts completely before glacier ice, due to the much larger surface area of fine-grained snow, which enhances heat transfer and accelerates melting.

Three coupled internal energy balance equations are solved, accounting for heat production from basal shear work and dissipation of fluctuation energy.

$$\partial_t(e_r) + \nabla \cdot (e_r \vec{u}_\phi) = \Phi_r \dot{E}_\phi + \xi_r \dot{E}_{\Sigma\to\phi} + \dot{q}_{ri} + \dot{q}_{rw} \tag{5.17}$$

$$\partial_t(e_{is}) + \nabla \cdot (e_{is} \vec{u}_\phi) = \Phi_{is} \dot{E}_\phi + \xi_{is} \dot{E}_{\Sigma\to\phi} - \dot{q}_{ri} + \dot{q}_{iw} - \dot{Q}_{m_i} \tag{5.18}$$

$$\partial_t(e_w) + \nabla \cdot (e_w \vec{u}_\phi) = \Phi_w \dot{E}_\phi + \xi_w \dot{E}_{\Sigma\to\phi} - \dot{q}_{rw} - \dot{q}_{iw} \tag{5.19}$$

where e_r, e_i, and e_w are the internal energies, defined by the specific heat capacity and the temperature. $\dot{Q}_{m_i}$ accounts for latent heat during phase changes and $\dot{E}_\phi$ represents sensible heat exchange (Munch et al., 2024).

The governing equations are solved numerically using a finite-volume method on a DEM. Two layers of ghost cells surround the computational domain to enable the implementation of boundary conditions. The spatial discretization employs a positivity-preserving HLL scheme, while time integration is performed using a Runge-Kutta-Heun scheme with an adaptive time stepping, determined by the Courant-Friedrichs-Lewy (CFL) condition, to ensure numerical stability. To prevent spurious oscillations, slope limiting is applied using a Minmod limiter (Christen, Kowalski, and Bartelt, 2010).

5.2 QGIS

QGIS is an open source geographic information system that has been useful for visualizing the results obtained with RAMMS. In particular, it was useful for creating the release area which was later used as input file for the numerical calculations. Furthermore, it was used for statistical analysis, using the Raster Calculator and Cell statistics tool to obtain the reach probability for each scenario. These parts will be explored in more detail in the next chapter. The images in this thesis are obtained from QGIS print layout.

5.3 R.RANDOMWALK

R.randomwalk is developed by the University of Graz. The model routes mass points from defined release raster cells, representing one or multiple mass movements, through a DEM until a predefined termination criterion is reached. It is defined as a flexible and multi-functional conceptual tool designed for both backward and forward analyses of mass movement propagation (Mergili, 2021).

For the Solatset Glacier, the model was applied by FMS, utilizing an empirical estimate of the runout angle as a function of release volume. This relationship was derived from a dataset of Alpine events (FMS, Paolo Perret, personal communication, 2026). The results from this application will be used for comparison with the outcomes of this thesis.

5.4 STATISTICAL ANALYSIS

Following the execution of all RAMMS simulations, the resulting datasets were further processed to quantify and visualize the influence of varying release parameters. The objective of the post-processing workflow was to derive a probabilistic avalanche hazard map based on the maximum core height, maximum velocity and maximum powder pressure.

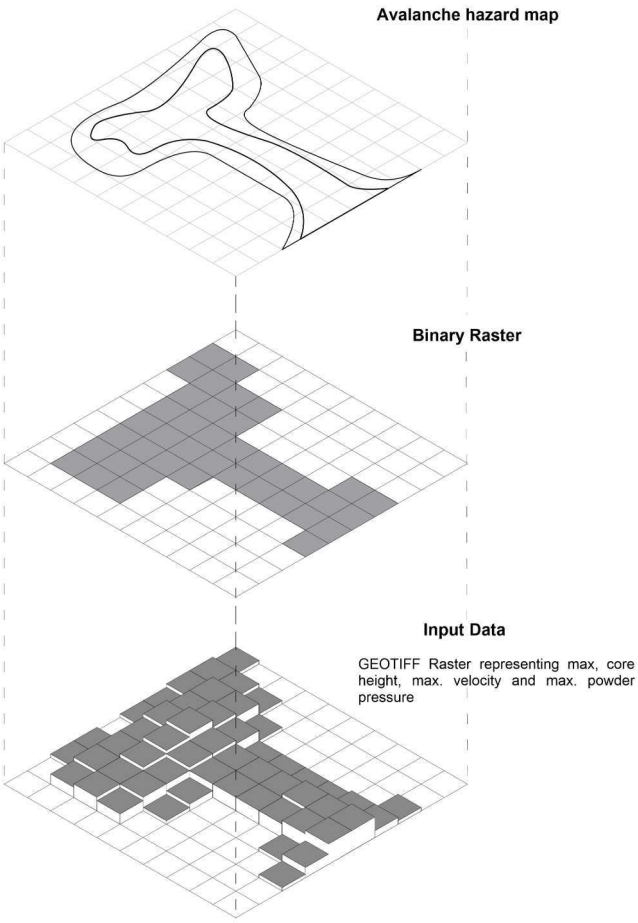

Figure 5.2: Statistical analysis

5.4.1 Binary classification of input data

For each simulation, the GeoTIFF raster layer representing the maximum core height, maximum velocity or maximum powder pressure was imported into QGIS. The original raster values were stored as continuous float64 data in meters, m/s and kPa. To enable statistical aggregation across simulations, each raster was reclassified into a binary format. This conversion assigned a value of 1 to pixels where the maximum core height exceeded a predefined threshold and 0 otherwise. The reclassification was performed using the QGIS Raster Calculator in combination with a Python script. The applied expression was:

$$(\text{"}A@1\text{"} > \text{threshold}) * 1 \tag{5.20}$$

where A represents the input raster. The output rasters were stored using the byte data type. This procedure was repeated for all simulations, resulting in 100 binary raster layers.

5.4.2 Computation of reach count

To quantify how often each pixel was affected across all simulations, the *Cell Statistics* algorithm in QGIS was applied. This tool computes a cell-by-cell function across multiple aligned raster layers. Using the 100 binary rasters as input, the sum was calculated for each pixel location. The resulting raster represents the reach count, i.e., the number of simulations (out of 100) in which the maximum core height exceeded 0.15 m at that pixel. The spatial resolution and extent of the output raster were defined using a common reference raster to ensure spatial consistency.

5.4.3 Derivation of the avalanche hazard map

Finally, the avalanche impact probability was calculated by normalizing the reach count raster. This was achieved using the Raster Calculator:

$$P = \frac{\text{reach count}}{100} \tag{5.21}$$

Each pixel value therefore represents the empirical probability (between 0 and 1) that, e.g., the maximum core height exceeds 0.15 m at that location. The resulting raster constitutes the probabilistic avalanche hazard map, which directly reflects the influence of variability in the release parameters across the ensemble of simulations.

5.5 RELEASE AREAS

The definition of potential release areas was conducted using QGIS. New shapefiles were generated for regions identified as prone to failure, utilizing the dedicated shape creation tools. The glacier thickness data, provided as a raster layer by FMS, served as the foundational dataset for this analysis. The workflow involved creating a shapefile for each candidate release area and calculating its surface area. Using the glacier thickness raster layer, the average depth of the glacier within each delineated area was computed. The volume of each potential release area was then estimated by multiplying the surface area by the average glacier depth. Multiple release areas were evaluated, and the final selection was based on both the physical plausibility of failure and the requirements of the modeling analysis.

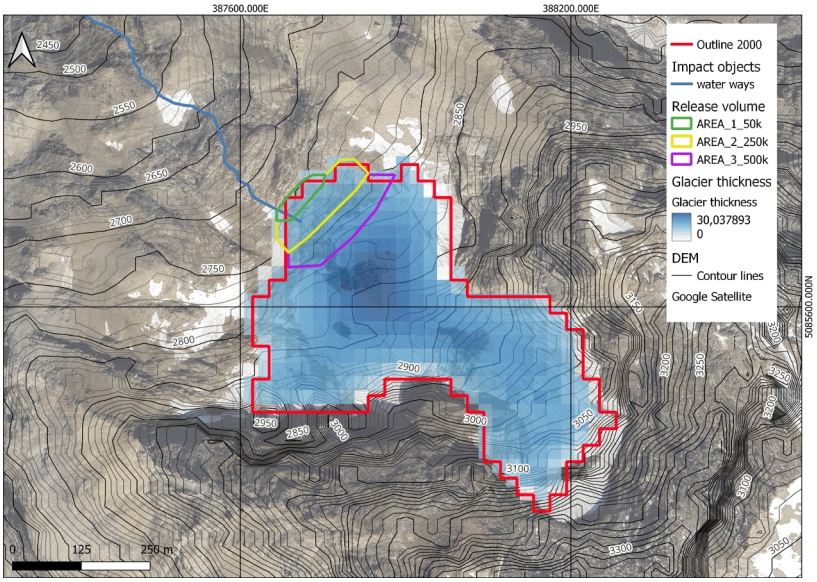

Figure 5.3: Solatset Glacier with three release areas

As illustrated in Fig.5.3, a waterway excites the glacier at a specific location, rendering this area significantly more unstable than surrounding regions. The presence of water influences glacier stability through multiple mechanisms: Highly saturated layers, such as those resulting from the entrainment of river water, can reduce basal resistance within the glacier. This reduction may lead to ruptures directly at the bedrock interface, particularly where the glacier slides over flowing water at the boundary between the glacier and the bedrock. Additionally, infiltrated and trapped meltwater within the glacier can trigger the opening of crevasses. The

infiltration of water also affects the extension of the temperate zone by releasing latent energy during freezing (Faillettaz, Funk, and Vincent, 2015). Furthermore, Fig.5.3 shows that the selected release area is situated within a steeper region, which increases the risk of failure particularly in the context of ramp-type failure (Noetzli et al., 2006). However, it is important to note that the physical processes underlying glacier instability are not yet fully understood. Consequently, the results of this analysis represent estimations rather than definitive ground truth, release masses can vary in volume and originate from different locations. For the Solatet Glacier, FMS conducted scenario analyses using r.randomwalk, proposing three release volumes: 50 000 m^3, 200 000 m^3, and 500 000 m^3. To align with their ongoing risk assessments and ensure comparability with their findings, a release volume of 239 336.21 m^3 and 503 383.91 m^3 was selected for this study.

6. BACK CALCULATION

Given that RAMMS is a physics-based model, it requires a substantial amount of input parameters. Beneath a DEM and the specifications of the release areas (as defined in the previous chapter), evaluating the best fitting calculation resolution is crucial in obtaining reliable results. Most critically, the model's accuracy hinges on the selection of appropriate friction parameters and other physical properties, which affect the behavior of the simulated avalanche. To address these uncertainties the Marmolada event 2022 was used as a reference for back calculation. This approach was necessary due to the absence of well-documented historical events at the Solatet Glacier that could serve as a basis for calibration.

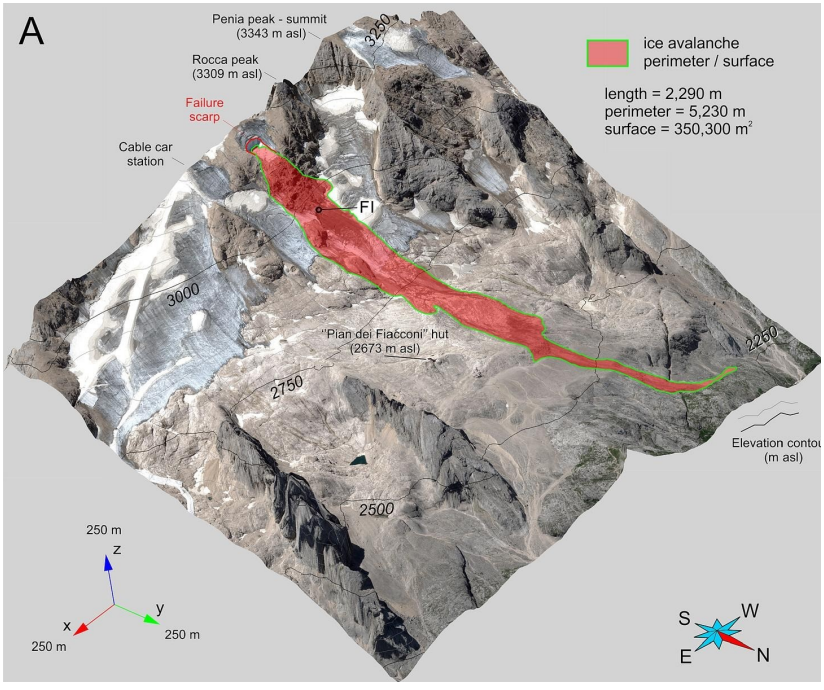

Figure 6.1: Overall view of the flow path (Bondesan and Francese, 2023)

The Marmolada collapse, a small, isolated glacier detachment just below Punta Rocca (3,309 m a.s.l.), occurred on July 3, 2022, resulting in 11 fatalities and 7 injuries. The avalanche traveled at speeds of 80–90 km/h over a distance of 2.3 km, ultimately depositing in a lateral valley at an elevation of 2,330 m a.s.l. Fig.6.1 shows the overall view of the flow path (Francese et al., 2024).

A comparative analysis of the Marmolada and Solatet glaciers (see Table 6.1) reveals similarities in their topographical characteristics. Given the well-documented nature of the Marmolada event, it provides a robust foundation for back-calculation, particularly in validating the flow path geometry as a qualitative criterion for model calibration.

Table 6.1: Comparison of Marmolada and Solatset glaciers.

	Marmolada glacier (Francese et al., 2024)	**Solatset glacier**
Slope angle	30°	31°
Exposure	Northern flank	North-west flank
Avalanche type	Ice-rock avalanche	Ice-rock avalanche
Volume	70400 m^3	50000 m^3, 200000 m^3, 500000 m^3
Elevation of release mass	3200 m	Ca. 2770 m

A total of 40 simulations were conducted to identify the optimal model configuration. For this purpose, key parameters, including friction coefficients, critical saturation levels, spatial resolution, water content, and curvature adjustments, were systematically varied. Appendix A provides informations on a detailed list of all input parameters. Among these simulations, four configurations (Figures 6.2) emerged as the best-fitting candidates, selected based on their alignment with the observed flow path.

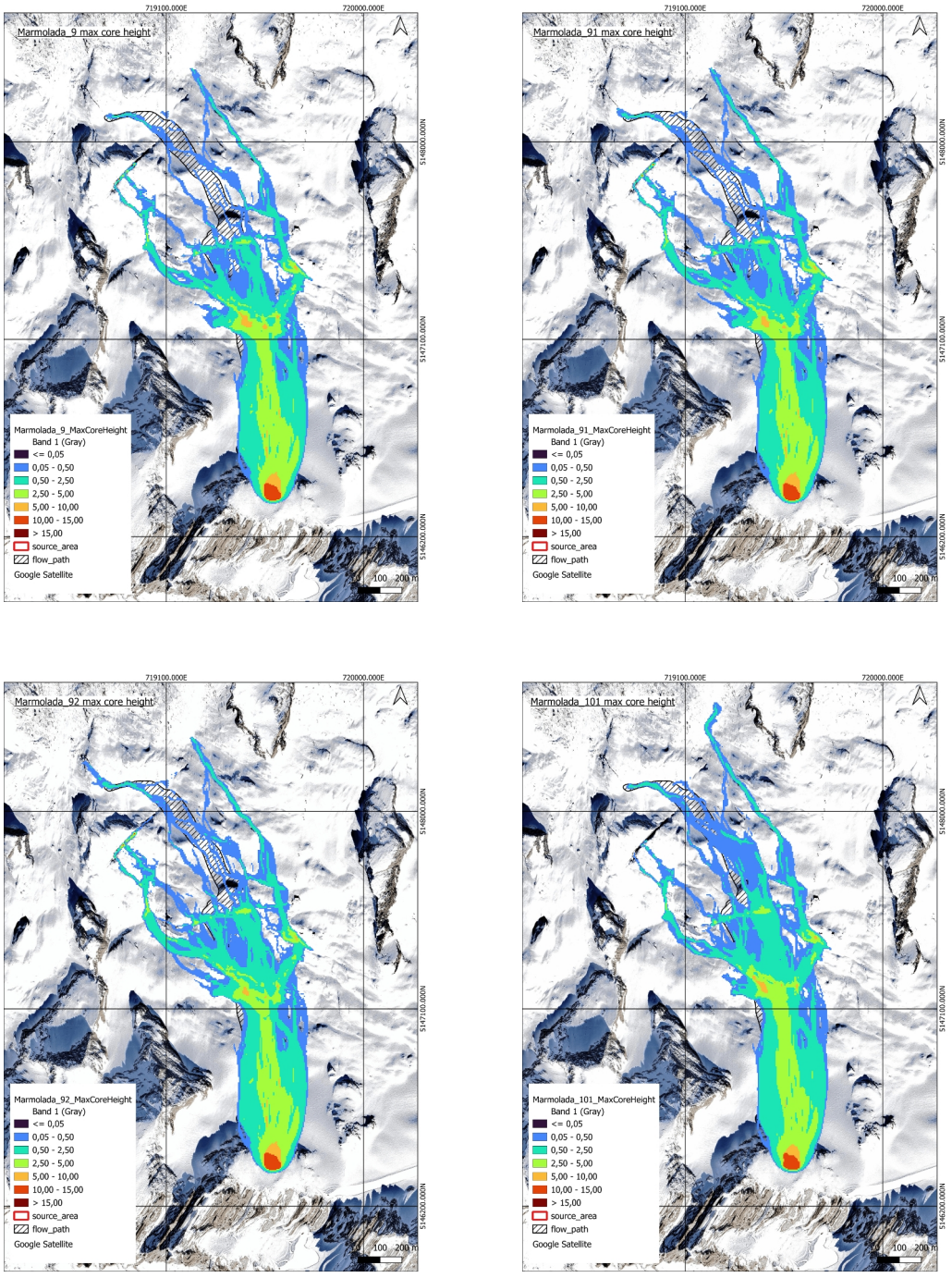

Figure 6.2: Max core height from Simulations 9, 91, 92, and 101 compared to the flow path of the Marmolada event

After comparing the simulated flow paths with the observed event, it is clear that while the model successfully reproduces the observed runout length it shows considerable lateral spreading, characterized by the development of multiple flow arms. However, these features are not evident in post-event documentation, such as photographs or video recordings ((Bondesan and Francese, 2023), (Olivieri and Bettanini, 2023), (Meteored, 2024)).
Two potential explanations have been proposed to account for this behavior. First, the mapped inundation area may not fully capture all the flow paths that were activated during the event. This discrepancy could arise because the RAMMS software emphasizes areas with higher flow heights or significant surface scarring, potentially overlooking regions with lower-intensity or more diffuse flow. Second, the lateral spreading observed in the simulations may be influenced by artifacts in the DEM. The one used in this study is a composite of datasets from 2009 and 2015, which may introduce topographic inconsistencies that affect the simulated flow behavior. Overall, RAMMS::RockIce demonstrates consistent behavior, but the results are subject to substantial uncertainties tied to terrain representation and event reconstruction. After considering all simulations, Simulation 9 was selected as the best fit due to its alignment with the observed flow characteristics. Consequently, the friction parameters derived from this simulation were adopted for modeling the Solatet Glacier event. In addition to a grid resolution of 5m the parameters which have been selected for winter and summer scenarios are visible in the respective chapters (Tables 7.1, 7.2, 8.1 and 8.2).

7. SUMMER SCENARIO

To account for uncertainties in the analysis, a statistical framework was implemented using the Monte Carlo method. This approach involved random sampling of two key parameters: the volumetric water content (Cw) of the release area and the critical saturation (Sc). These parameters were varied to reflect climate change impacts, such as changing temperature and precipitation patterns, which influence water availability and saturation levels in glacial environments. Cw as well as Sc were modeled using a Beta-PERT distribution, which is widely used for representing expert estimates. Unlike the triangular distribution, the mean of the Beta-PERT distribution is four times more sensitive to the most likely value than to the minimum and maximum values, reducing potential systematic biases that can skew mean values. The resulting probability distribution function (PDF) of the water content is shown in Figure 7.1 and were derived using the Beta-PERT formula:

$$f(x|a,b,m) = \begin{cases} \frac{(x-a)^{\alpha-1}(b-x)^{\beta-1}}{B(\alpha,\beta)(b-a)^{\alpha+\beta-1}} & \text{for } a \leq x \leq b \\ 0 & \text{otherwise} \end{cases} \tag{7.1}$$

where a is the minimum value, b is the maximum value, m is the most likely value, and α and β are shape parameters calculated as:

$$\alpha = 1 + 4 \cdot \frac{m-a}{b-a} \tag{7.2}$$

$$\beta = 1 + 4 \cdot \frac{b-m}{b-a} \tag{7.3}$$

and $B(\alpha, \beta)$ is the Beta function.

The cumulative distribution function (CDF) of the Beta-PERT distribution is given by:

$$F(x|a,b,m) = I_{\frac{x-a}{b-a}}(\alpha, \beta) \tag{7.4}$$

where $I_x(\alpha, \beta)$ is the regularized incomplete Beta function (Farnum and Stanton, 1987).

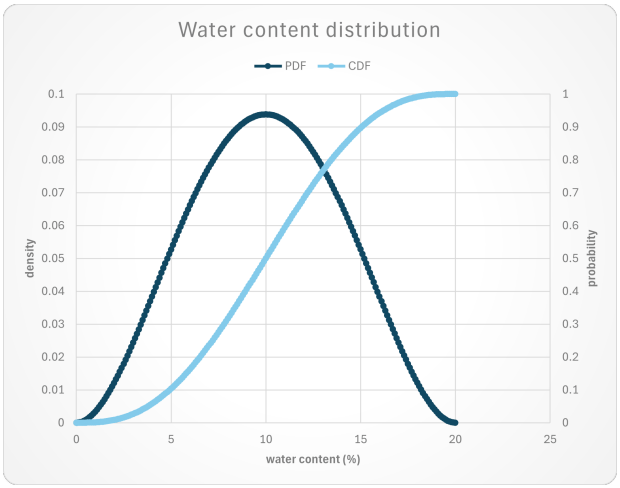

Figure 7.1: PDF and CDF of the release mass water content

For this study, the volumetric water content was defined with the following parameters:

- Minimum value: 0%
- Most likely value: 10%
- Maximum value: 20%

The maximum value was defined based on the observations from the Marmolada 2022 event (Francese et al., 2024) while the most likely value was derived from calibration values commonly used in back-calculations, outlined in the RAMMS user manual (RAMMS AG, personal communication, 2026).

To further refine the relationship between Cw and ice temperature, we incorporated findings from Ryser et al. (2013), which demonstrate that the water content in ice is proportional to the square of the water vein diameters in cold ice. The analysis reveals that the ice water content increases systematically as the temperature approaches the pressure melting temperature (PMT), as illustrated in Figure 7.2.

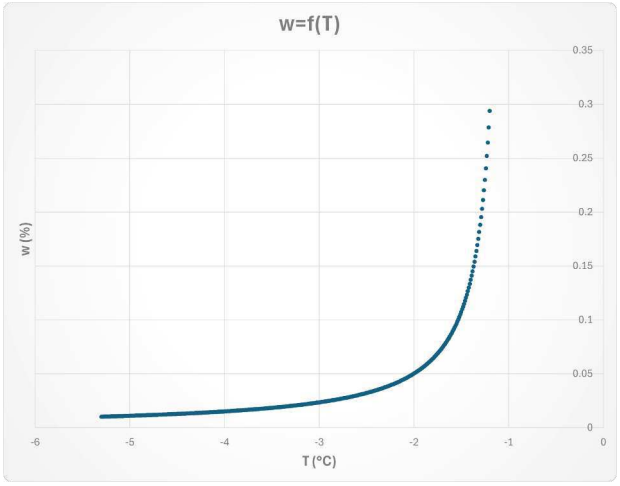

Figure 7.2: Water content as a function of the temperature

The interstitial water volume between ice grains can be described as a function of temperature, where θ represents the difference between the ice temperature and the melting temperature of ice (set to -1°C by RAMMS).

$$\omega = C'|\Theta|^{-1.1} \tag{7.5}$$

The constant C' is dependent on the density of intracrystalline veins, and consequently, it varies with both ice density and soluble impurity concentration. As demonstrated by Ryser et al. (2013), a value of C' = 0.05 yields significantly higher water content compared to C' = 0.01 for the same Θ. To accurately represent the physical conditions of the Solatet Glacier, a value of C' = 0.05 was selected for our simulations. Similarly, the critical saturation (Sc) was sampled randomly between 0.4 and 0.6 using the Beta-PERT distribution, with the most likely value set to 0.5. The resulting PDF and CDF are shown in Figure 7.3.

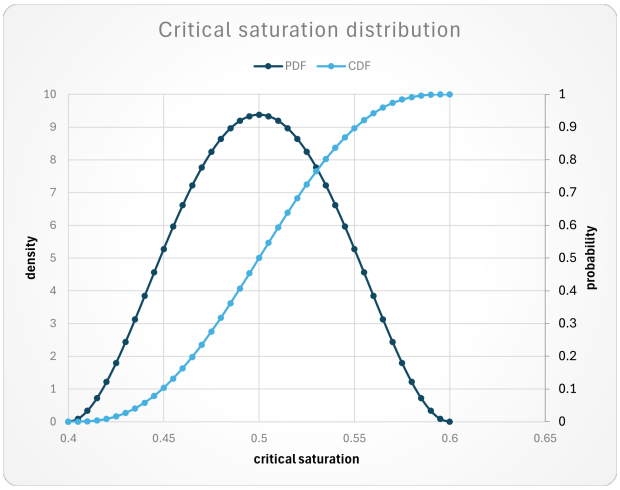

Figure 7.3: PDF and CDF of the critical saturation

The selected parameter range was based on recommendations from an unpublished draft of the RAMMS user manual (RAMMS AG, personal communication, 2026) and preliminary findings from Zhuang et al. (RAMMS AG, personal communication, 2026). These drafts provided modeling and research results for different scenarios, guiding the calibration of simulation parameters. The statistical framework was implemented using Monte Carlo simulations, generating 100 random probability values for both Cw and Sc, from a range between 0 and 1. The ice temperature was then derived from these values using the established relationship between θ and ice water content. Appendix A provides informations on a detailed list of all input parameters. Tables 7.1 and 7.2 list the selected friction parameters for the summer scenario simulations. Additional parameters required for the simulation were suggested by model developers, based on back-calculations from several events (RAMMS AG, personal communication, 2026).

Table 7.1: Fixed material properties for rock, ice, and snow in the summer scenario

	Rock	**Ice**	**Snow**
Xi (m/s^2)	500	1000	2000
Mu	0.55	0.35	0.32
Cohesion (Pa)	200	100	50
Activation energy (kj/m^2)	10	4	2

Table 7.2: Fixed capillary and pore pressure properties in the summer scenario

	Capillary	**Pore pressure**
Xi (m/s^2)	500	500
Mu	0.2	0.05
Softening (m)	0.25	0.05

To complete the simulation setup, the following assumptions were made:

- Volumetric content of rock: 10%
- Volumetric content of snow: 0%
- Volumetric content of ice: 1 - (rock + water)
- Rock density: 2500 kg/m^3
- CoVolume density: 1200 kg/m^3

8. WINTER SCENARIO

Evans and Clague proposed a theory highlighting the significant influence of the glacial environment on the runout distance of rapid mass movements, particularly as they travel across low-friction surfaces such as glaciers, melted ice, or snow. Given this influence, scenarios involving snow cover are of particular interest for further investigation (Schneider et al., 2011). Therefore, the parameter settings required adjustments to reflect seasonal conditions. While the distribution of water content and its relationship with ice temperature remained consistent with the summer scenario, the range of the water content PERT distribution was modified to account for lower water content values expected during winter. The updated parameters for the PERT distribution are a minimum value of 0.01%, most likely value of 2.5% and a maximum value of 5%. This adjustment results in the PDF and CDF which can be represented by the following curves:

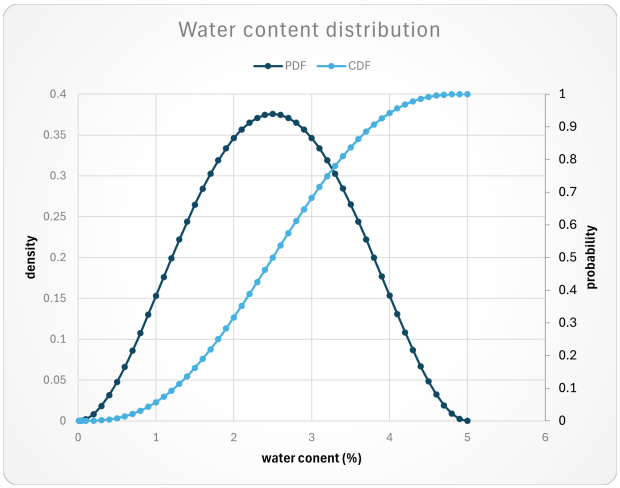

Figure 8.1: PDF and CDF of the release mass water content

To accurately represent the winter scenario, additional parameters related to snow cover were introduced and fixed. One critical parameter is the erosion depth of the snow cover,

which varies depending on seasonal conditions. Similar to the water content distribution, the erosion depth was modeled using a PERT distribution, based on expert knowledge. The parameters for this distribution are:

- Minimum value: 0.5 m
- Most likely value: 1.5 m
- Maximum value: 2.5 m

The corresponding PDF and CDF for the erosion depth is illustrated in Figure 8.2.

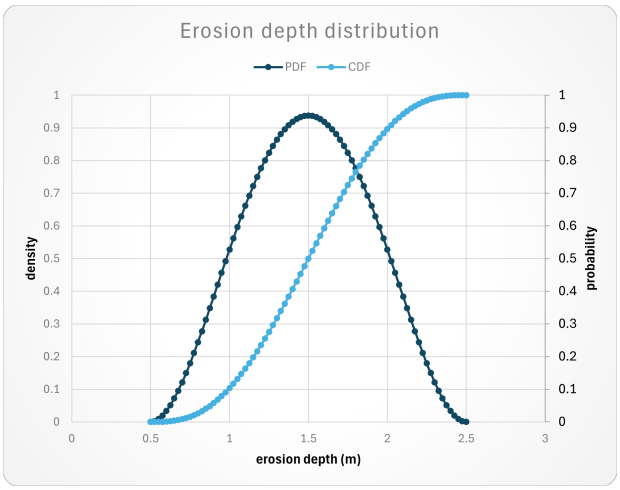

Figure 8.2: PDF and CDF of the snow erosion depth

Furthermore, the density and temperature of the release mass are critical factors in determining avalanche dynamics. To refine and explain the parameter setup, two extreme-case scenarios were considered: First, when the rock-ice avalanche travels over a "firn" layer, a highly dense, compacted snow that is difficult to entrain. Second, when the avalanche entrains the snow cover, which has a significantly lower density. To account for these differences, a relationship between erosion depth and snow density had to be established. Jonas, Marty, and Magnusson (2009) identified four key factors influencing the bulk density of snow: season, snow depth (equivalent to erosion depth in the RAMMS setup), site altitude, and region. Their findings are based on the assumption that input factors should be easily obtainable during erosion depth measurements. The results are presented in look-up tables, where three variables can be selected to achieve the best fit. The underlying relationship is

described by the equation:

$$\rho b = a \cdot HS + b + \text{offset} \tag{8.1}$$

Here, a and b are variables that depend on altitude and season, while the offset accounts for regional location. For the Solatet Glacier scenario, the following relationship was chosen:

$$\rho b = 46 \times HS + 217 - 1.1 \tag{8.2}$$

This equation represents conditions at an altitude > 2000 m in February. For simplicity, this relationship was applied uniformly across all winter scenario simulations. Since the study by Jonas, Marty, and Magnusson (2009) was conducted using data exclusively from Switzerland, the regional parameter was selected to match the Wallis canton, the closest analogue to the study area. Unlike the summer scenario, the release area parameters for the winter scenario are based on the difference between the release mass of the glacier and the release mass including the additional snow volume, calculated using the erosion depth. This additional snow volume, represented by the snow cover on top of the glacier as well as the snow cover along the slope that is entrained due to erosion mechanisms, leads to an increased release volume. To finalize the simulation setup, the following assumptions were made, primarily based on results obtained from back-calculation and recommendations provided by RAMMS AG. Additional parameters required for the simulation were suggested by model developers, based on back-calculations from several events (RAMMS AG, personal communication, 2026). A significant difference from the summer scenario is the modification of the friction parameters (Mu and Xi), which is due to the flow over low-friction surfaces.

- Volumetric content of rock: 10% (of the glacier release mass)
- Rock density: 2500 kg/m^3
- CoVolume density: 1200 kg/m^3

Table 8.1: Fixed material properties for rock, ice, and snow in the winter scenario

	Rock	**Ice**	**Snow**
Xi (m/s^2)	1000	1000	2000
Mu	0.32	0.32	0.32
Cohesion (Pa)	200	100	50
Activation energy (kj/m^2)	10	4	2

Table 8.2: Fixed capillary and pore pressure properties in the winter scenario

	Capillary	**Pore pressure**
Xi (m/s^2)	500	500
Mu	0.2	0.05
Softening (m)	0.25	0.05

The statistical framework was implemented in the same way as for the summer scenario. Appendix A provides informations on a detailed list of all input parameters.

9. RESULTS

9.1 REACH PROBABILITY ANALYSIS

The reach probability of the modelled rock-ice avalanches for the 240 000m^3 and 500 000m^3 summer scenario as well as the same release volumes for a winter scenario, are illustrated in Figures 9.1. Every result uses a 15cm threshold and is derived from the max core height.

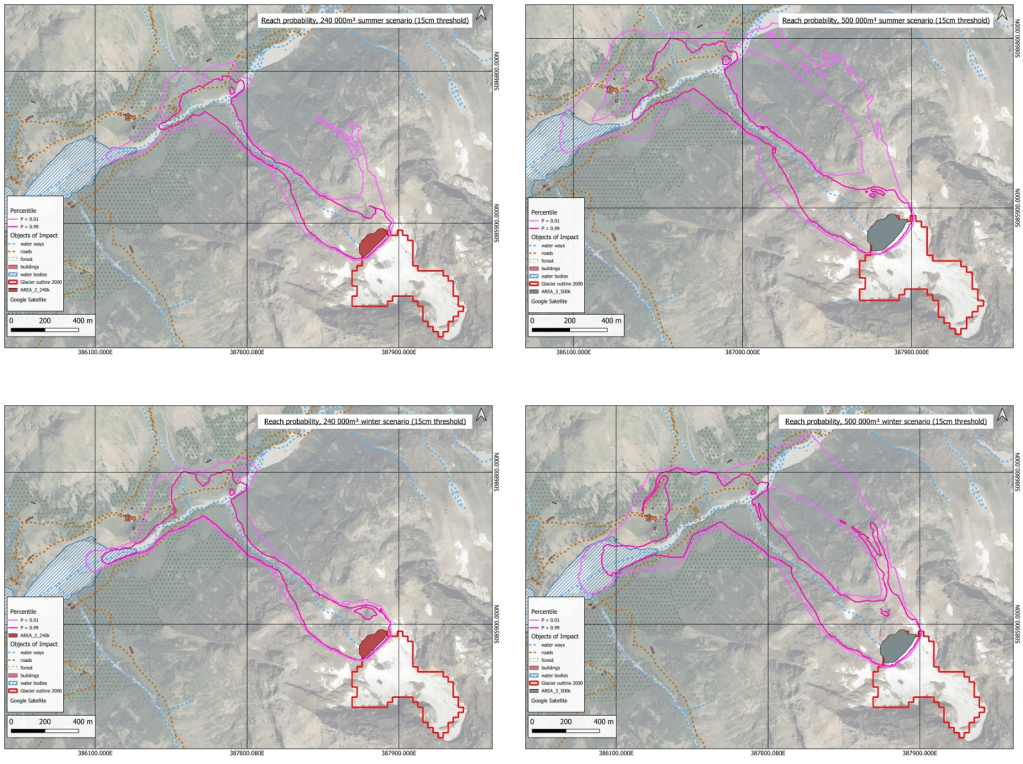

Figure 9.1: Reach probability of all four scenarios

The maps display the spatial distribution of the avalanche's potential reach, with the 1st

and 99th percentiles highlighted in magenta. These percentiles represent the minimum and maximum expected extents of the avalanche, respectively. The red outline delimits the area of the Solatset Glacier, which serves as the source zone for the avalanche. The Figures reveal that the avalanche's path extends downstream from the glacier following a mountain stream until it reaches the river valley, with the 99th percentile enclosing an area that includes waterways, roads, forest, and buildings. The difference between the magenta lines indicate the region where the avalanche is likely to propagate (98% of all tested avalanches), with the 99th percentile covering a larger spatial extent compared to the 1st percentile. This suggests a variability in the potential reach of the avalanche, depending on the specific conditions of the avalanche.

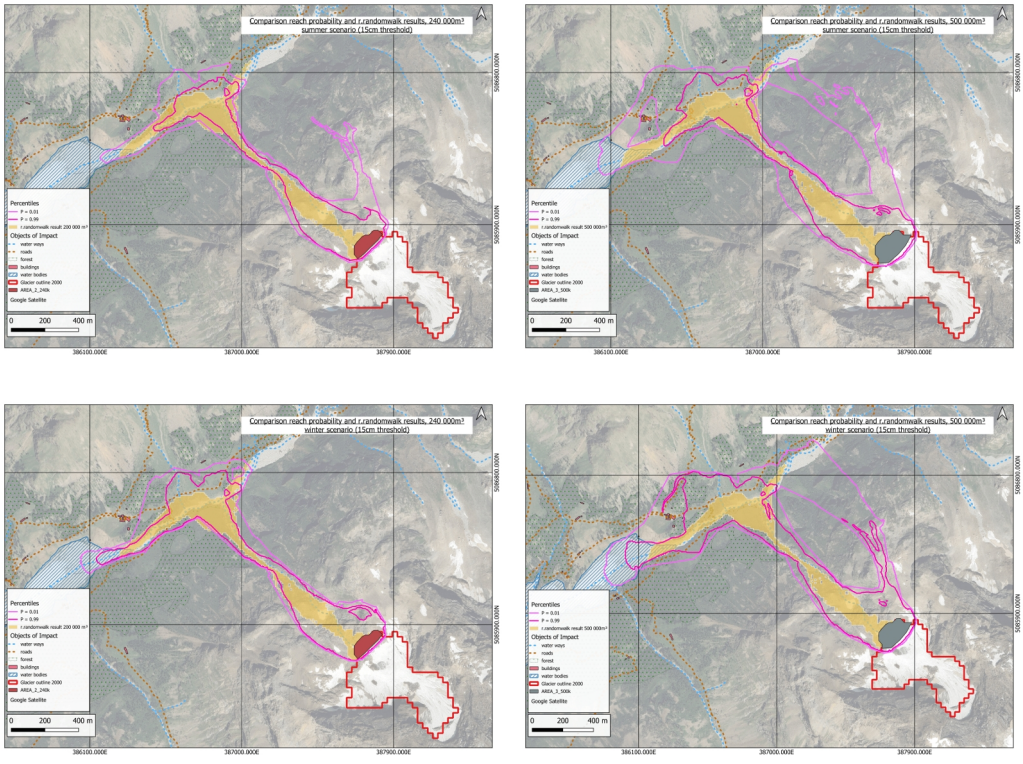

Figure 9.2: Comparison of the reach probability and the results from FMS for all four scenarios

Figures 9.2 provides a comparative analysis of the reach probability results obtained from the RAMMS model and the results obtained by FMS using r.randomwalk, developed by

the University of Graz. The yellow shading represents the FMS results for a 200 $000m^3$ release volume, while the magenta lines again denote the 1st and 99th percentiles from the RAMMS model. A notable observation is the general alignment between the RAMMS 1st percentile and the r.randomwalk results, particularly in the central and downstream regions of the avalanche path. However, discrepancies between the two results become particularly evident as the avalanche reaches the valley bottom.

For the 240 $000m^3$ scenario, both in summer and winter, the r.randomwalk results extend further to the right (upstream), while the maximum expected extent obtained with the RAMMS model reaches further to the left (downstream). This discrepancy is more pronounced in the winter scenario compared to the summer scenario. In the 500 $000m^3$ scenario, the horizontal extent of the avalanche reach is significantly larger in the RAMMS results, with this difference being even more developed in the winter scenario. Additionally, a notable difference in lateral spreading and counter-slope run-up is observed across all four scenarios. The development of a secondary flow path is already evident in the 240 $000m^3$ summer scenario, becoming even more significant in the 500 $000m^3$ scenarios for both seasons. Suggesting that additional areas outside the primary avalanche channel may be at risk, especially for high-volume scenarios. These variations underscore the influence of release volume and seasonal conditions on avalanche dynamics, as captured by the two models.

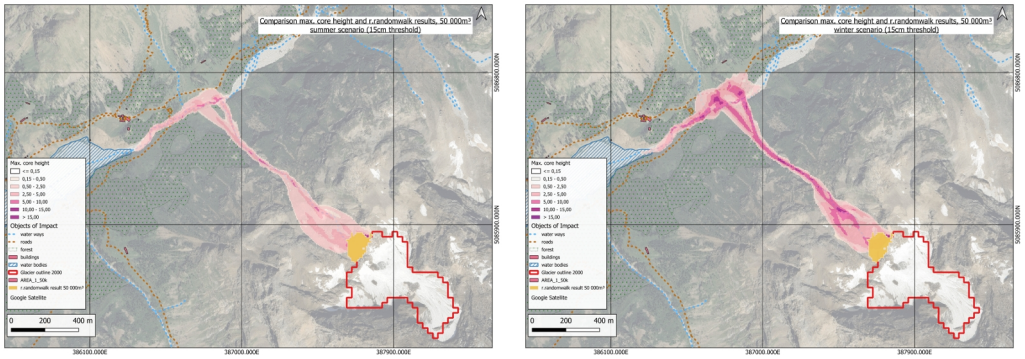

Figure 9.3: Max. core height of the 50 $000m^3$ winter and summer scenario with a threshold of 15cm, including the result obtained using r.randomwalk

The maximum core height for the 50 $000m^3$ release volume is presented in Figures 9.3 comparing the results for summer and winter scenarios. These maps were made from a single simulation using the average values for the varying input parameters. The maps illustrate

the spatial extent and magnitude of the avalanche's core height, with the pink shading indicating areas where the core height reaches different values. Within the summer scenario, the maximum core height is concentrated along the main avalanche path where also the highest values occur. The lateral spread is relatively confined. The maximum core height in the winter scenario extends further downstream compared to the summer scenario, indicating a longer runout distance. Together with a higher core height it suggests a greater potential for impact and damage in this area. The lateral spread of the avalanche in winter conditions is broader, particularly in the valley bottom together with a stronger counter slope run-up.
A major difference is observed between the results obtained in this thesis and those generated using the r.randomwalk tool. The flow in the r.randomwalk simulations stops shortly after release, which can be attributed to the use of a very high runout angle for a low release volume (FMS, Paolo Perret, personal communication, 2026). This discrepancy represents the largest divergence between the RAMMS results and those obtained with r.randomwalk, particularly when compared to simulations using the other two release volumes.

9.2 VELOCITY ANALYSIS

The velocity distribution for each avalanche scenario is presented in Figures 9.4, illustrating the 1st and 99th percentiles of velocities exceeding 5 m/s and 10 m/s for both the 240 $000m^3$ and 500 $000m^3$ release volumes under summer and winter conditions. The selection of these velocity thresholds is based on their relevance to hazard assessment. Specifically, a velocity of 10 m/s represents the threshold for snow avalanches (with a density of 300kg/m^3), corresponding to a pressure threshold of 30 kPa, a critical value in hazard mapping according to Swiss and Valle d'Aosta legislation (FOEN, 2021). However, for the co-volume density of 1200kg/m^3 relevant to this study, the same pressure threshold is reached at a lower velocity of 5 m/s. This approach provides a clear spatial visualization of areas where the avalanche attains significant velocities, thereby enabling a robust identification of hazardous zones associated with high-velocity impacts.

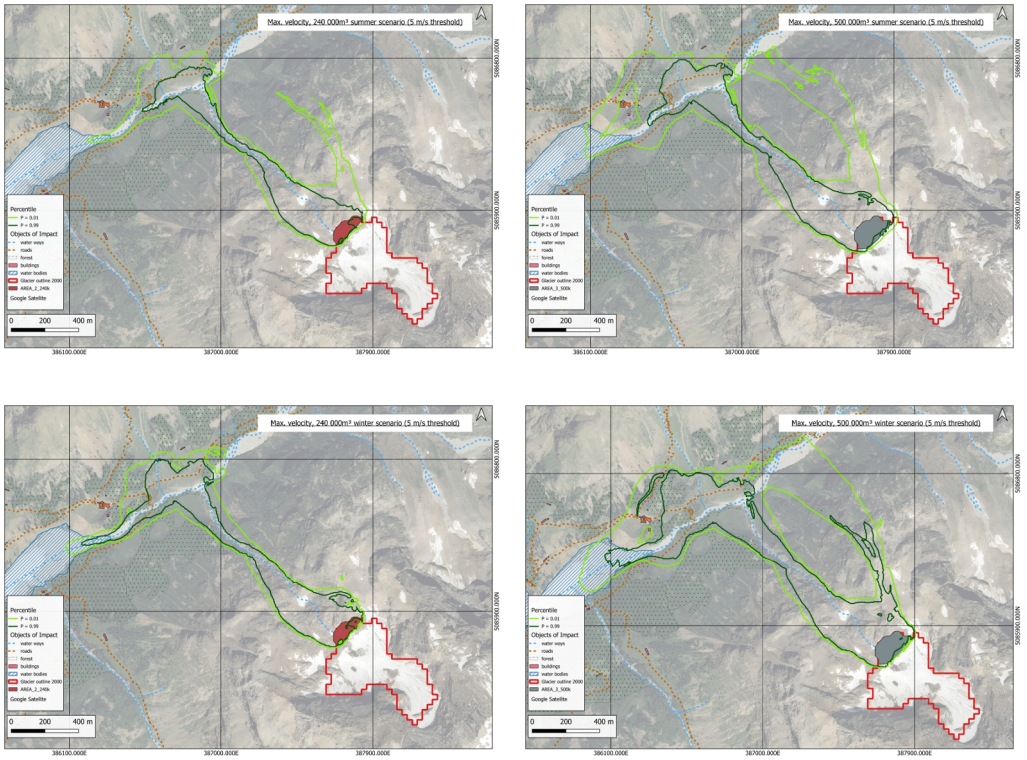

Figure 9.4: Velocity distribution of all four scenarios with a threshold of 5 m/s

The 1st percentile (dark green lines) represents the minimum expected extent of velocities exceeding the threshold, while the 99th percentile (light green lines) visualizes the maximum expected extent of velocities exceeding the threshold. This indicates that 98% of all simulated avalanches have velocities exceeding the threshold in the area between these two percentiles. Consequently, this data allows for an assessment of the spatial variability in avalanche velocity under different conditions. In both winter and summer scenario results, the 99th percentile exceeds further downstream in the valley bottom compared to the 1st percentile. A notable difference between summer and winter results is the reach of the 1st percentile, which indicates higher velocities in the winter avalanche flow at points downstream where the summer avalanche has already slowed down. Additionally, the difference between the 1st and 99th percentiles is less pronounced in the winter scenario, suggesting a smaller range of velocity values. This could likely be attributed to reduced surface friction on snow-covered terrain. The potential range of avalanche velocities demonstrates how release volume and seasonal conditions influence the spatial extent of high-velocity zones. An increase in release volume results in a more extensive spatial distribution of areas exceeding the velocity threshold, particularly in the winter scenario. The avalanche reaches further downstream, and the lateral spread of high velocities is more significant.

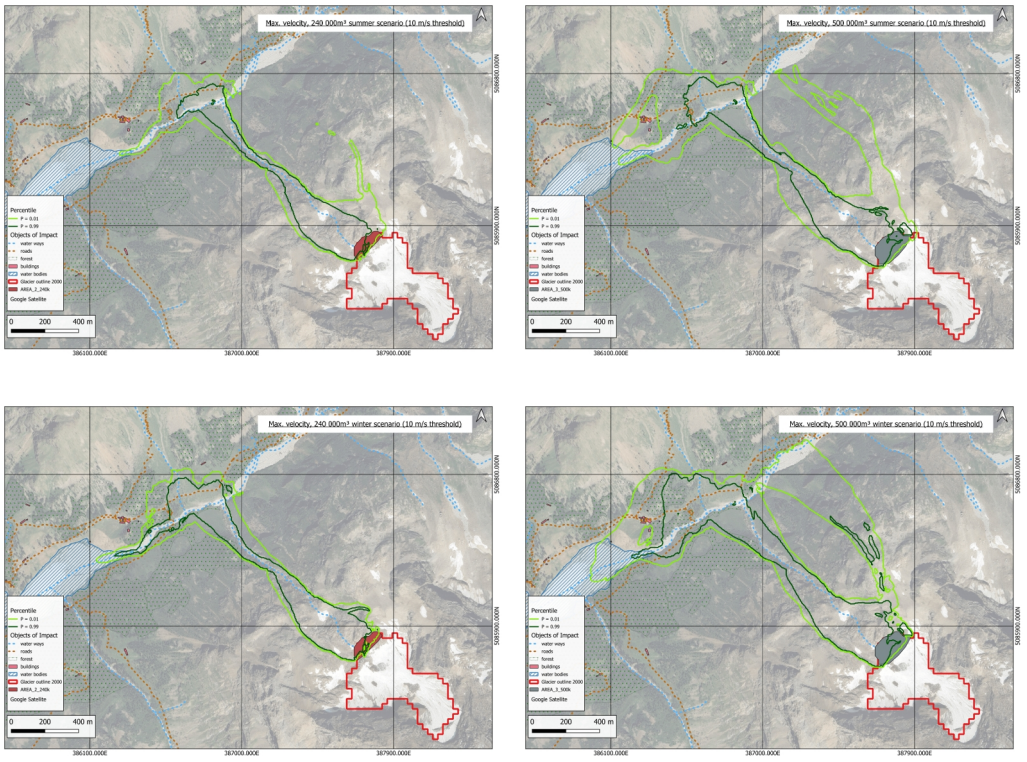

Figure 9.5: Velocity distribution of all four scenarios with a threshold of 10m/s

When comparing the results for the 5 m/s and 10 m/s (visible in Figures 9.5) thresholds, only a small difference in reach is visible. However, lateral spreading and the presence of secondary flow paths persist, suggesting that these flow paths maintain significant velocities.

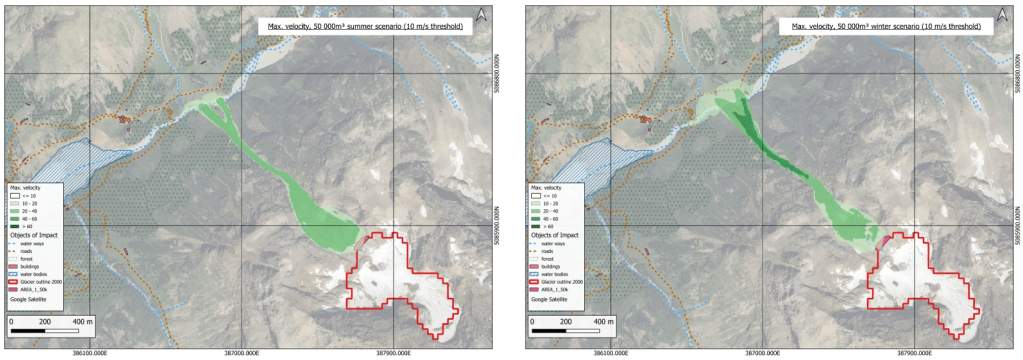

Figure 9.6: Max. velocity of the 50 000m^3 winter and summer scenario with a threshold of 10m/s

The maximum velocity of the flow along the path for the 50 000m^3 release volume are presented in Figures 9.6, comparing the results for the winter and summer scenarios. The green shading highlights areas where the avalanche velocity exceeds the 10 m/s threshold. In the summer scenario, the maximum velocity is predominantly concentrated along the main avalanche path, with limited lateral spreading upon reaching the valley bottom. The highest velocities are observed within this central path, indicating a more confined and localized flow. In contrast, the winter scenario not only exceeds the 10 m/s threshold along the same main path as the summer scenario but also demonstrates greater lateral spreading and a longer downstream reach into the valley bottom. The peak velocities in the winter scenario are located in the lower section of the main avalanche path. Compared to the summer scenario, the winter scenario exhibits higher mobility, characterized by a more extensive spatial distribution of velocities and higher maximum values. This increased mobility is likely attributable to reduced surface friction on snow-covered terrain.

9.3 POWDER PRESSURE ANALYSIS

Figures 9.7 shows the distribution of powder cloud pressures exceeding 0.5kPa, a threshold below which pressures are comparable to storm-force winds (0.5kPa corresponds to the stagnation pressure of wind with a velocity slightly above 30 m/s) and therefore they can be considered negligible for avalanche hazard assessment (Prof. Dr. Massimiliano Barbolini, personal communication, 2026). This value marks the lower limit for distinguishing hazardous powder cloud effects from background wind loads. Additionally, the 3 kPa threshold, visible in Figures 9.8, represents a reference value for powder cloud pressure hazard

mapping, as it can cause damage to the lowest quality of constructions (Munch et al., 2024). The 1st and 99th percentile is illustrated for the 240 $000m^3$ and 500 $000m^3$ release volumes under summer and winter conditions. It defines the areas below the Solatset glacier which are potentially affected by high pressure values due to avalanches and therefore show hazardous areas since pressure can lead to structural damage.

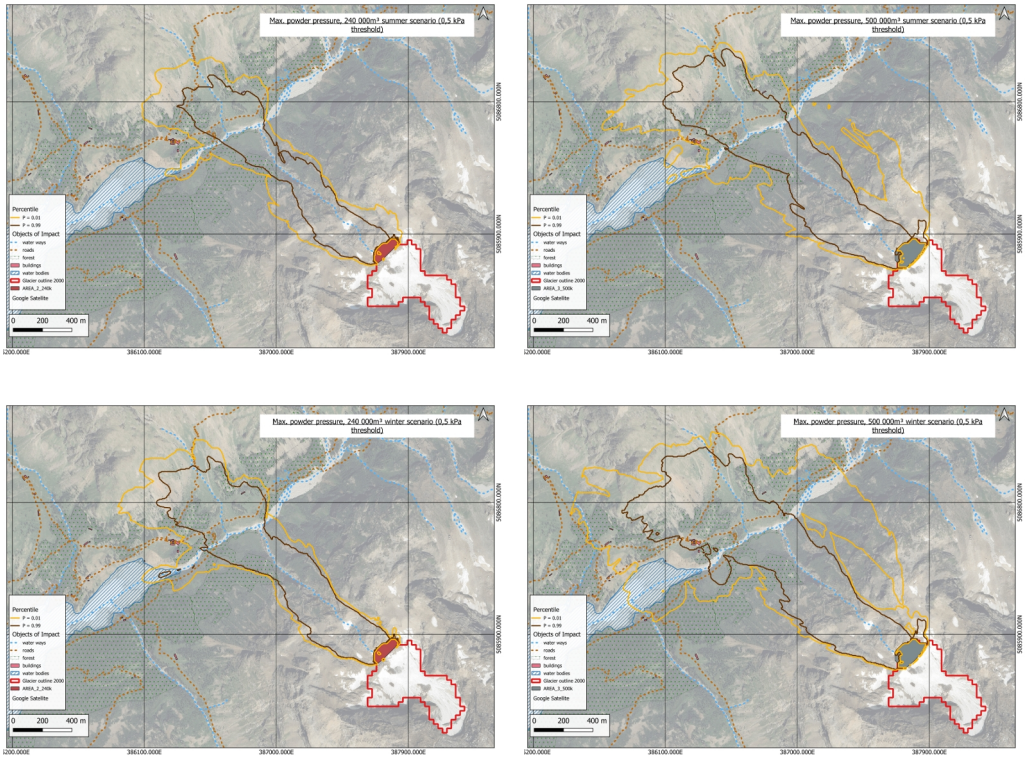

Figure 9.7: Powder pressure distribution of all four scenarios with a threshold of 0.5kPa

The 1st percentile (brown lines) represents the minimum expected extent of pressure exceeding the threshold, while the 99th percentile (light orange lines) visualizes the maximum expected extent of powder pressures exceeding the threshold. This indicates that 98% of all simulated avalanches generate powder pressures above the threshold in the area between these two percentiles. The areas within the 1st percentile are generally confined to the upper and middle sections of the avalanche path, while the 99th percentile areas extend further downstream, laterally and counter slope, particularly in the valley bottom. Especially the

winter scenario exhibits a significantly wider lateral spread of high pressures. Secondary "powder" paths, where pressure exceeds the threshold, are only visible in the winter season which increases with a larger release volume. In general, the increase of release mass results in a more extensive spatial distribution of areas exceeding the pressure threshold. The powder cloud reaches further up on the counter slope, reflecting the influence of the larger release volumes.

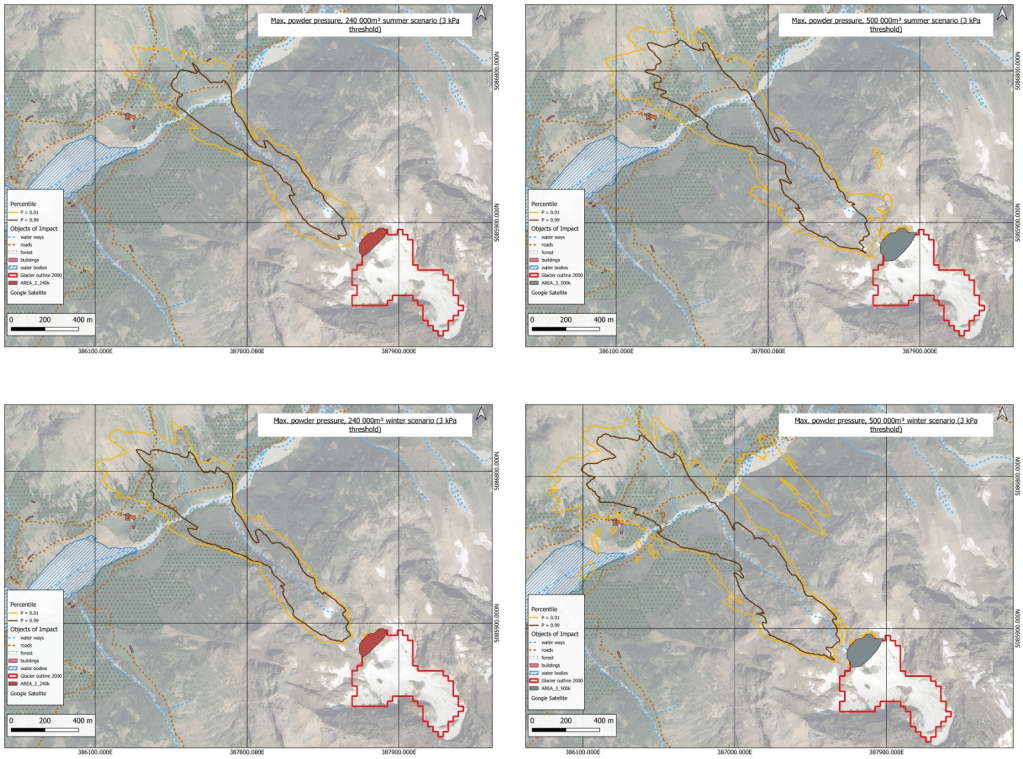

Figure 9.8: Powder pressure distribution of all four scenarios with a threshold of 3kPa

When comparing the results of the 0.5 kPa and 3 kPa (Figures 9.8) thresholds, the spatial extent of areas exceeding the pressure threshold is smaller for the 3 kPa threshold. However, lateral spreading and counter slope run up persist even at the higher threshold, suggesting that these areas experience significant pressure regardless of the threshold. The presence of secondary "powder" arms is less significant than for the smaller threshold. The difference between the 1st and 99th percentiles is more pronounced for the 0.5 kPa threshold,

indicating a wider range of pressure values across the avalanche path.

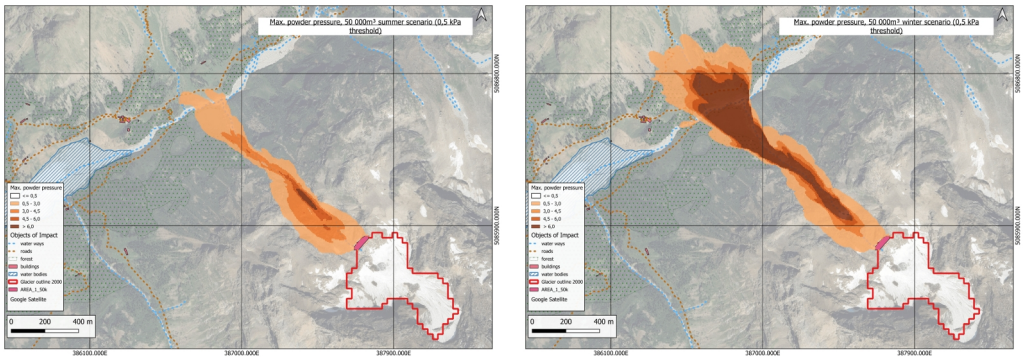

Figure 9.9: Max. powder pressure of the 50 000m^3 winter and summer scenario with a threshold of 0.5kPa

The maximum powder pressure of the 50 000m^3 release mass flow along the path are illustrated in Figures 9.9, comparing the results for the summer and winter scenarios using a 0.5 kPa threshold. The values are represented using brown shading, with darker shades indicating higher pressure levels. In the summer scenario, the powder pressure distribution is minimal and highly concentrated within the main avalanche path. There is limited lateral spreading and negligible counter-slope run-up. The highest pressure values are localized in the upper section of the powder cloud, close to the release area. In contrast, the winter scenario exhibits a significantly larger spatial extent of powder pressure. While the maximum pressure values are distributed along the entire main avalanche path, the lateral spreading is much more pronounced compared to the summer scenario. Additionally, a strong counter-slope run-up is evident. High pressure values extend to the valley bottom, affecting areas containing roads and forests.

9.4 PEARSON CORRELATION

The Pearson correlation analysis was conducted to examine the relationship between ice temperature and runout distance across four avalanche scenarios. The results revealed significant correlations in all scenarios, though the strength of these relationships varied notably between seasons and release volumes. The relationship is visualized through scatter plots (Figures 9.10) for each of the four scenarios. These plots reveal two notable trends. First, there is a stronger positive correlation between increasing ice temperature and runout dis-

tance in the summer scenarios compared to the winter scenarios, indicating that warmer ice temperatures in summer contribute to longer avalanche runout distances. Second, the data points exhibit a pronounced clustering pattern, with over 95% of the results concentrated in a specific area. This suggests that, despite variations in ice temperature, the majority of simulated avalanches terminate within a similar spatial range, implying a consistent collapse zone across the different scenarios.

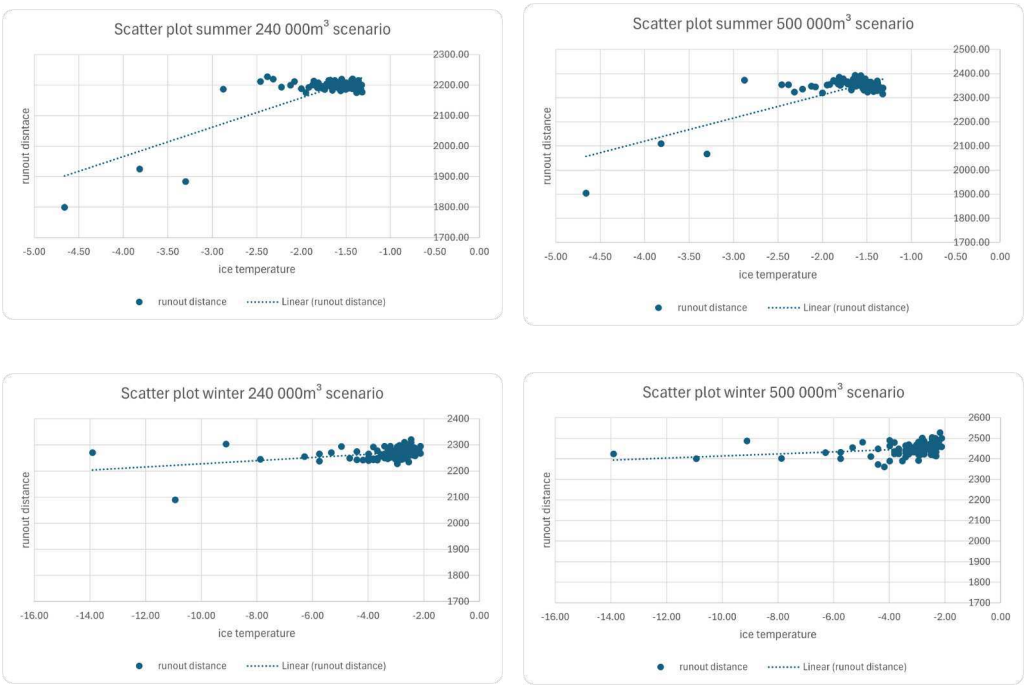

Figure 9.10: Scatter plots for each scenario representing the correlation of runout distance and ice temperature

In the summer scenarios, the analysis identified a strong positive correlation between ice temperature and runout distance. For the 240 000m^3 release volume, the Pearson correlation coefficient was r(98) = 0.80 (p < .001), indicating that increasing ice temperatures are strongly associated with longer avalanche runout distances. Similarly, the 500 000m^3 release volume in summer conditions showed a nearly identical strong correlation, with r(98) = 0.78 (p < .001). These findings suggest that during summer, ice temperature plays a critical role in determining how far an avalanche travels.

In contrast, the winter scenarios exhibited weaker yet still significant correlations. For the 240 000m^3 release volume, the correlation coefficient was r(98) = 0.41 (p < .001), indicating a moderate positive relationship between ice temperature and runout distance. Meanwhile, the 500 000m^3 release volume in winter conditions showed an even weaker, though still significant, correlation of r(98) = 0.28 (p = .005). The reduced strength of these correlations suggests that while ice temperature remains a factor in winter, its influence on runout distance is less pronounced compared to summer.

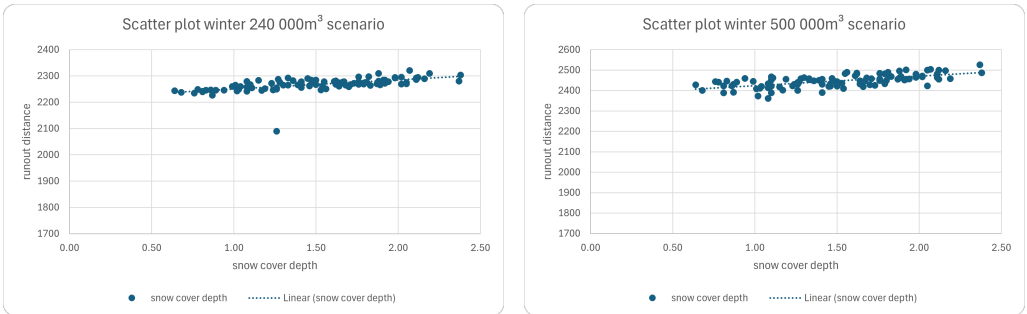

Figure 9.11: Scatter plots for each scenario representing the correlation of runout distance and snow cover depth

A significant correlation exists between the runout distance and the depth of the erodible snow layer in the winter scenarios (see Figures 9.11). This relationship is supported by Pearson correlation coefficients of r(98) = 0.65, p < .001 for the 500 000m^3 release volume and r(98) = 0.58, p < .001 for the 240 000m^3 scenario. However, in terms of absolute increase of runout distance the effect is not as relevant as the one we found for summer scenarios, where water content plays a dominant role. This is probably due to the negative correlation considered in this work between the depth of the snow cover and its density.

10. DISCUSSION

This study analyzed how varying volumetric contents within the release mass, their associated physical parameters, seasonal conditions, and release volume influence rock-ice avalanche dynamics at the Solatset Glacier. Using reach probability, velocity distribution, powder pressure distribution, and Pearson correlation analyses, the results reveal that release volume is the primary driver of runout distance, surpassing the impact of seasonal conditions. Larger release volumes not only extend runout distances but also increase lateral spreading and hazard potential, particularly beyond the main avalanche path. These findings align with previous research by Oberndorfer, Fischer, and Fuchs (2026), who demonstrated that avalanche release volume significantly influences both spatial coverage and linear propagation, though their results also highlighted the importance of site-specific characteristics. Additionally, studies have shown that higher ice content in avalanches reduces the friction coefficient linearly, increasing the potential for damage and casualties due to interactions between ice, snow, and water (Noetzli et al., 2006).

When comparing the scenario results from this study to those generated using r.randomwalk, significant differences emerge only for the lowest release volume (50 $000m^3$), where the RAMMS approach employed in this thesis yields more realistic outcomes. While runout distances for higher release volumes along the main valley remain relatively consistent between the two models, RAMMS simulations reveal a substantially greater potential runout on the opposite side of the valley. This discrepancy underscores the importance of physics-based models like RAMMS in capturing complex avalanche behaviors, particularly lateral spreading, compared to non-physics-based tools like r.randomwalk, which rely on flow routing algorithms and predefined stopping criteria. Winter conditions further amplify runout distances compared to summer scenarios, likely due to reduced surface friction, though this effect remains secondary to the influence of release volume. While release volume strongly influences runout distance, its effect on velocity and powder pressure is minimal. Instead, seasonal conditions produce the most pronounced differences, particularly at the 1st per-

centile. For instance, while differences in velocity and powder pressure between release volumes are not significant, the variations between the same release volume under different seasonal conditions are substantial. The increased velocity values could be attributed to low-frictional surfaces such as glaciers, melting ice, or snow that enhance the mobility of rapid mass movements (Schneider et al., 2011).

The increased powder pressure in winter may be linked to the formation of a larger powder cloud, driven by the additional snow volume in winter scenarios. However, according to expert knowledge, fluidization of the avalanche core and the presence of suspendable fine material, such as snow and ice, are critical for generating strong powder clouds. In contrast, denser avalanches, such as those with a high rock content, fluidize less and produce weaker air blasts, as rocks are harder to suspend and entrain into the cloud. Thus, the explanation for the larger powder cloud in winter scenarios is likely the presence of lower density material within the avalanche compared to summer scenarios, which facilitates the incorporation of material into the cloud. These findings are based on empirical evidence ((Zhuang et al. (2024)), (Zhuang et al. (2025)), (Zhuang et al. (2024)) and (Bartelt et al., 2016)).

The Pearson correlation analysis further revealed that ice temperature, and thus water content within the release mass has less influence on runout distance in winter scenarios. This suggests that the observed increase in runout is driven by factors other than initial water content alone, such as frictional heating, which can generate meltwater during avalanche motion. Many authors have proposed that meltwater production enhances the mobility of the rock phase and may even trigger transitions to fluid-saturated debris flows (Munch et al., 2024). To further investigate this theory the production of meltwater within the avalanche core should be observed using the RAMMS software. Additionally, the limited variation in water content in winter scenarios (0–5%) may explain its reduced influence on runout distance. Future research should investigate additional parameters that could affect winter runout, such as snowpack properties.

In contrast, summer scenarios demonstrate a strong positive correlation between runout distance and ice temperature, indicating that higher water content, resulting from warmer ice, plays a critical role in extending avalanche mobility. This aligns with Schneider et al. (2011), who noted that water at the avalanche base can reduce internal friction through mechanisms such as hydroplaning or pore pressure buildup.

A further analysis of the simulation results revealed less dispersion in the scatter plots than anticipated, a pattern that influences the results of the Pearson correlation analysis. Several factors may contribute to this outcome. First, the assumption of symmetrical distributions

(beta-PERT) for random variables, selected based on expert knowledge, may not fully capture the natural variability present in rock-ice avalanches. Exploring alternative distributions could potentially yield more realistic results and refine the observed correlations. Second, the predefined ranges for critical variables, such as initial water content or meltwater production during avalanche motion, may require further validation. While a more detailed analysis is necessary to assess these ranges, obtaining precise field data remains challenging due to the dynamic and complex nature of avalanche processes. Additionally, the limited number of simulations (100 per scenario), constrained by time and computational resources, may have influenced the observed clustering. Increasing the number of simulations could provide deeper insights into result variability and strengthen the robustness of the correlation analysis. Finally, topographical constraints along the avalanche path may also explain the clustered data patterns.

11. CONCLUSION

The ongoing impacts of global climate change present growing challenges for mountainous regions, particularly through the alteration of glacier dynamics and the emergence of new natural hazards. Since the beginning of the 21st century, the rapid retreat of glaciers and the degradation of permafrost have significantly influenced slope stability, hydrological regimes, and geomorphological processes, thereby affecting interactions across the hydrosphere, atmosphere, biosphere, and lithosphere (Cuffey and Paterson (2010), and Benn and Evans (2010)). While these broader impacts are well-documented, the specific role of inherent uncertainties in simulating complex natural processes, such as rock-ice avalanches, remains relatively unexplored. A comprehensive literature review revealed that while statistical approaches have been applied to other mass-movement processes, no prior studies have focused on a statistical evaluation of rock-ice avalanche dynamics. Due to the absence of well-documented historical events at the Solatset Glacier, a back-calculation approach was adopted, using the Marmolada 2022 event as a reference.

This thesis investigated how uncertainties in initial material composition and seasonal conditions influence rock–ice avalanche dynamics at the Solatset Glacier using the RAMMS modelling framework combined with a probabilistic approach.The results clearly show that release volume is the primary control on avalanche reach and impact area. Larger release volumes significantly increase runout distance, lateral spreading, and the likelihood of secondary flow paths. This highlights the importance of accurately constraining potential release volumes in hazard assessments. At the same time, seasonal conditions strongly influence flow characteristics, particularly velocity and powder pressure. Winter scenarios exhibit enhanced mobility, broader spreading, and more extensive pressure impact zones due to reduced friction and snow entrainment. These effects are critical for risk evaluation, as they directly affect damage potential even when runout distances are comparable. Nevertheless, it should be highlighted that in winter conditions, the collapse of glacier portion is less likely to occur (apart from those due to cascading effects, like triggering due to collapses of rocky

spurs overlooking the glaciers).
A key finding of this study is the strong dependence of runout distance on water content in summer conditions, demonstrated by high correlations between ice temperature (directly related to water content) and runout. In contrast, this relationship is much weaker in winter, indicating that different physical mechanisms dominate under snow-covered conditions. This suggests that future climate warming may particularly increase summer avalanche mobility through enhanced meltwater production.
The comparison with r.randomwalk demonstrates that physics-based models provide a more comprehensive representation of avalanche behaviour, especially for capturing lateral spreading and complex flow patterns. In addition, the number of outcomes related to physical properties of the flow physic-based models is essential for realistic hazard and risk mapping in complex terrain. Finally, the probabilistic framework reveals that while parameter uncertainty influences avalanche behaviour, topography imposes a strong constraint on the overall runout domain, leading to clustered termination zones. This emphasizes the need to consider both terrain controls and process variability in hazard assessments. In conclusion, this study advances the understanding of rock–ice avalanche dynamics by:

- Quantifying the relative importance of release volume, water content, and seasonal conditions,
- Demonstrating the value of probabilistic simulation approaches,
- Highlighting the limitations of simplified modelling methods.

Future work should focus on improving input data quality (e.g. updated glacier geometry), increasing simulation sample size, and incorporating additional physical processes such as dynamic meltwater production. Furthermore, additional studies should investigate the cross-correlation between water content and critical saturation. Since this relationship has not yet been demonstrated in previous research, no cross-correlation was determined for this study. Applying the same modelling approach on a less topographically constrained study case would be useful for further investigating the potential effects of uncertainties on avalanche runout distances and the affected areas.
These steps will further enhance the predictive capability of rock–ice avalanche models and support more reliable hazard assessment in a changing climate.

REFERENCES

Alean, J. (1985). "Ice avalanches: some empirical infromation about their formation and reach". In: *Journal of Glaciology*.

Barbolini, M. and Savi, F. (2001). "Estimate of uncertainties in avalanche hazard mapping". In: *Annals of Glaciology, 32, pp. 299-305*.

Bartelt, P. et al. (2016). "Configurational energy and the formation of mixed flowing/powder snow and ice avalanches". In: *Annals of Glaciology, 57(71), pp. 179-188*.

Bionaz, Comune di (2025). *A Bionaz si trova una delle dighe più grandi d'Europa*. URL: `https://comune.bionaz.ao.it/novita/la-diga-di-place-moulin/` (visited on 02/17/2026).

Bondesan, A. and Francese, R. (2023). "The climate-driven disaster of the Marmolada Glacier (Italy)". In: *Geomorphology Volume 431, 108687*.

Christen, M., Kowalski, J., and Bartelt, P. (2010). "RAMMS: Numerical simulation of dense snow avalanches in three-dimensional terrain". In: *Cold Regions Science and Technology Volume 63, Issues 1–2, pp. 1-14*.

Cuffey, K. and Paterson, W. (2010). *The Physics of Glaciers*. Academic Press.

Evans, S. et al. (2009). "Catastrophic detachment and high-velocity long-runout flow of Kolka Glacier, Caucasus Mountains, Russia in 2002". In: *Geomorphology 105, pp. 314–321*.

Faillettaz, J., Funk, M., and Vincent, C. (2015). "Avalanching glacier instabilities: Review on processes and early warning perspectives". In: *Review of Geophysics 53, pp. 203–224*.

Fan, X. et al. (2022). "Imminent threat of rock–ice avalanches in High Mountain Asia". In: *Nature Reviews Earth & Environment, Science of the Total Environment 836, 155380*.

Fan, X. et al. (2025). "The Friction Behavior of Rock□ Ice Avalanches in Relation to Rock□ Ice Segregation: Insights From Flume Physical Experiments". In: *JGR Earth Surface 130, e2024JF007904*.

Farinotti, D. et al. (2025). "Fact sheet for the now-collapsed Birchgletscher, Switzerland". In: *ETH Zurich*.

Farnum, N. and Stanton, L. (1987). "Some Results Concerning the Estimation of Beta Distribution Parameters in PERT". In: *The Journal of the Operational Research Society, Vol. 38, No. 3, pp. 287-290*.

FOEN (2021). *EconoMe, Wirksamkeit und Wirtschaftlichkeit von Schutzmassnahmen gegen Naturgefahren*. URL: `https://econome.ch/eco_work/index.php` (visited on 04/13/2026).

Francese, R. et al. (2024). "Failure of Marmolada Glacier (Dolomites, Italy) in 2022: Data-based back analysis of possible collapse mechanisms as related to recent morpho-climatic evolution and possible trigger factors". In: *EGU*.

Giani, A. (2026). *Glaciers of Valpelline Valley (Grand Combin)*. URL: `https://www.summitpost.org/glaciers-of-valpelline-valley-grand-combin/885785` (visited on 02/17/2026).

Google, Earth (2026). URL: `https://comune.bionaz.ao.it/novita/la-diga-di-place-moulin/` (visited on 04/10/2026).

Huggel, C., Kääb, A., and Haeberli, W. (2004). "An assessment procedure for glacial hazards in the Swiss Alps". In: *Canadian Geotechnical Journal*.

Jacquemart, M. et al. (2024). "Detecting the impact of climate change on alpine mass movements in observational records from the European Alps". In: *Earth Science Reviews 258, 104886*.

Jonas, T., Marty, C., and Magnusson, J. (2009). "Estimating the snow water equivalent from snow depth measurements in the Swiss Alps". In: *Journal of Hydrology 378, pp. 161–167*.

Mergili, M. (2021). *r.randomwalk - The landslide routing tool. r.randomwalk 2.1 User manual*. URL: `https://www.randomwalk.org/manual.php` (visited on 04/13/2026).

Meteored (2024). *Tragödie in der Marmolada (Italien), als ein Teil eines Gletschers abbrach*. Accessed: 2026-03-18. URL: `https://www.youtube.com/watch?v=KavjJaQtbug`.

Munch, P. et al. (2024). "Dynamic thermo-mechanical modelling of rock–ice avalanches". In: *JGR Earth Surface 129, e2024JF007805*.

Noetzli, J. et al. (2006). "GIS-based modelling of rock-ice avalanches from Alpine permafrost areas". In: *Computational Geosciences 10, pp. 161–178*.

Oberndorfer, S., Fischer, J., and Fuchs, S. (2026). "Quantifying the influence of avalanche release volume on runout probability: A case study of a mountain road section". In: *Cold Regions Science and Technology, Volume 242*.

Olivieri, L. and Bettanini, C. (2023). "Preliminary observation of Marmolada glacier collapse of July 2022 with space-based cameras". In: *Remote Sensing Letters 14:1, pp. 21-29*.

Ryser, C. et al. (2013). "Cold ice in the ablation zone: Its relation to glacier hydrology and ice water content". In: *Journal of Geophysical Research: Earth Surface 118(2)*.

Schneider, D. et al. (2011). "Unravelling driving factors for large rock–ice avalanche mobility". In: *Earth Surface Processes and Landforms 36, pp. 1948–1966*.

UZH (2007). "Dealing with natural hazards: Ice Avalanches". In: *Swiss virtual campus*.

Zhong, Y. et al. (2024). "Large rock and ice avalanches frequently produce cascading processes in High Mountain Asia". In: *Geomorphology 449, 109048*.

Zhuang, Y., Bartelt, P., et al. (2024). "Rock avalanche-induced air blasts: implications for landslide risk assessments". In: *Geomorphology, 452, 109111, 11 pp.*

Zhuang, Y., Dash, R. K., et al. (2025). "Fluidization and snow cover effects in rock-ice-snow avalanches: lessons from Piz Cengalo, Fluchthorn, and Piz Scerscen events". In: *Computers and Geotechnics, 186, 107456, 13 pp.*

Zhuang, Y., Dawadi, B., et al. (2024). "An earthquake-triggered avalanche in Nepal in 2015 was exacerbated by climate variability and snowfall anomalies". In: *Communications Earth and Environment, 5(1), 456, 10 pp.*

A. APPENDIX: SIMULATION PARAMETERS

Due to the extensive volume of simulation inputs, they are only available upon request. Interested readers are encouraged to contact the author directly at `kappler.anne@web.de`. Please specify the purpose of the request to facilitate the provision of relevant materials.